J. Fluid Mech. (2008), *vol.* 612, *pp.* 107–141.
doi:10.1017/S0022112008002978 Printed in the United Kingdom

Low-dimensional characteristics of a transonic jet. Part 1. Proper orthogonal decomposition

C. E. TINNEY[1], M. N. GLAUSER[2] AND L. S. UKEILEY[3]

[1]Department of Aerospace Engineering & Engineering Mechanics, University of Texas at Austin, Austin, TX 78712, USA

[2]Department of Mechanical & Aerospace Engineering, Syracuse University, Syracuse, NY 13244, USA

[3]Department of Mechanical & Aerospace Engineering, University of Florida, Shalimar, FL 32579, USA

(Received 14 November 2006 and in revised form 4 June 2008)

An experimental investigation concerning the most energetic turbulent features of the flow exiting from an axisymmetric converging nozzle at Mach 0.85 and ambient temperature is discussed using planar optical measurement techniques. The arrangement of the particle image velocimetry (PIV) system allows for all three components of the velocity field to be captured along the (r, θ)-plane of the jet at discrete streamwise locations between $x/D = 3.0$ and 8.0 in 0.25 diameter increments. The ensemble-averaged (time-suppressed) two-point full Reynolds stress matrix is constructed from which the integral eigenvalue problem of the proper orthogonal decomposition (POD) is applied using both scalar and vector forms of the technique. A grid sensitivity study indicates that the POD eigenvalues converge safely to within 1 % of their expected value when the discretization of the spatial grid is less than 30 % of the integral length scale or 10 % of the shear-layer width. The first POD eigenvalue from the scalar decomposition of the streamwise component is shown to agree with previous investigations for a range of Reynolds numbers and Mach numbers with a peak in azimuthal mode 5 at $x/D = 3.0$, and a gradual shift to azimuthal mode 2 by $x/D = 8.0$. The eigenvalues from the scalar POD of the radial and azimuthal components are shown to be much lower-dimensional with most of their energy residing in the first few azimuthal modes, that is modes 0, 1 and 2, with little change in the relative energies along the streamwise direction. From the vector decomposition, the azimuthal eigenspectra of the first two POD modes shift from a peak in azimuthal mode 5 at $x/D = 3.0$, followed by a gradual decay to azimuthal mode 2 at $x/D = 8.0$, the differences in the peak energies being very subtle. The conclusion from these findings is that when the Mach number is subsonic and the Reynolds number sufficiently large, the structure of the turbulent jet behaves independently of these factors.

1. Introduction

Large-scale turbulent structures have been known for some time now to govern a moderate to large percentage of the overall turbulent kinetic energy in most flows (Townsend 1956; Brown & Roshko 1974; Winant & Browand 1974). Trying to capture the spatial and temporal evolution of these structures has become paramount to understanding the process by which heat, mass and momentum are transferred through the mean flow and has become the subject of numerous investigations,

expressly to those concerning thermal and fluid flow type phenomena. In particular, the importance of these large-scale structures to the production of noise in high subsonic and even supersonic jet flows remains an important and timely topic of scientific and engineering interest.

In general, jet noise is created by the turbulent mixing of a high-speed (high-temperature) jet exhaust plume with the ambient air, thus creating massive pressure fluctuations in the near-field and ultimately large acoustic signatures in the far-field regions of the flow. The broad range of frequencies associated with the entire process comprises high frequencies at the jet exit (because of the relatively 'small-scale' turbulent structures in the flow at this location†) and lower frequencies emanating around a region after the close of the potential core (larger-scale events). The sound intensity is known to be directional owing to the competing effects of convection and refraction of the sources in the jet shear layer (Ribner 1969), with the greatest levels radiating at shallow angles to the jet axis (typically around 30°). Since most of the turbulent kinetic energy of the flow is governed by the large-scale structures, it is advantageous for us to extract these underlying events from the chaotic turbulence, because of the importance of these events to the sound-generation process (e.g. Michalke & Fuchs 1975; Ffowcs Williams & Kempton 1978; Juve, Sunyach & Comte-Bellot 1980; Bastin, Lafon & Candel 1997; Seiner 1998; Tam 1998; Freund 2001).

A number of techniques have been proposed for extracting, or separating 'large-scale' structures from the background turbulence (see Bonnet *et al.* 1998, for a comparison of different coherent structure eduction methods). In the current investigation, the methods adopted are based on Lumley's (1967) proper orthogonal decomposition (POD) since it is well suited for inhomogeneous systems. While the POD does not necessarily select physical structures, it does re-project data onto a basis set that has been optimized with respect to the Reynolds stress characteristics of the turbulence. Therefore, with many applications of the POD technique to transitional and turbulent flows, (e.g. Glauser 1987; Moin & Moser 1989; Delville *et al.* 1999; Citriniti & George 2000; Caraballo *et al.* 2003; Noack, Papas & Monkewitz 2005; Tinney *et al.* 2006*b*), care must be taken when interpreting POD modes with regard to physical structures. For details of the POD's mathematical construction, its historical applications to turbulent flows, as well its relation to other modelling techniques, i.e. Galerkin projection, linear stochastic estimation, pattern recognition and others, see Berkooz, Holmes & Lumley (1993).

The application of the POD to the axisymmetric shear layer was first documented by the seminal work of Glauser (1987) and Glauser & George (1987) who showed that the dominant basis function (first POD mode) contained 40 % of the resolved turbulent kinetic energy, with an additional 40 % of the energy found in the next two modes combined. Glauser (1987) postulated a 'model' for the most energetic flow events in the jet that invoked a streamwise interaction between two axisymmetric vortices, and followed their evolution to explain the higher azimuthal structure, guided by measurements in the radial and azimuthal plane of the jet. An extension to this work was later performed by Citriniti & George (2000) to show the life cycle of the large-scale dynamics near the end of the potential core, the most prominent being a 'volcano-like' bursting event that ejected high streamwise momentum fluid

† The structures that comprise the production region of the energy spectrum near the nozzle exit are considered small in relation to the events downstream, but are locally large-scale turbulent events.

through the core, thus inducing a high-strain series of counter-rotating vortex pairs. The investigation of Citriniti & George (2000) used the POD to filter out small-scale fluctuations capable of obscuring the interpretation of the interactions between the more energetic events in the turbulent shear layer. In doing so, 67 % of the resolvable flow field's energy was captured with the first POD mode alone.

Ukeiley, Seiner & Ponton (1999) and Taylor, Ukeiley & Glauser (2001) performed similar studies using CTA tools in the (r, θ)-plane of a Mach 0.3 and 0.6 jet, thus characterizing (for the first time) the streamwise evolution of the most energetic Fourier-azimuthal modes in the compressible jet's shear layer and its dynamical characteristics from a linear stochastic estimation (LSE) procedure. Likewise the first POD mode contained 40 % of the mean square mass-flux and the distribution of the azimuthal modal energy evolved from a broad spectral distribution of modal energy at $x/D = 4$, to a much narrower peak in the lower modes 1,2 and 3 at $x/D = 8$. Further measurements were conducted at Mach 0.85, although because of high probe breakage, the decomposition technique could not be applied to the higher Mach number flow. Comparisons were made, and similarities were found in the spectral measurements at all Mach numbers (0.30, 0.60 and 0.85), suggesting similarity in the POD solution for all of the conditions studied. Succeeding the compressible jet studies, Jung, Gamard & George (2004) and Gamard, Jung & George (2004) demonstrated a similar modal evolution in the incompressible jet, thus fortifying the results between the incompressible and compressible jet flows under a range of Mach numbers and Reynolds numbers and the lack of Reynolds-number dependence on the energy distribution of the first POD mode. The latter of these two studies demonstrated how the fluctuating streamwise velocity stabilized asymptotically to Fourier-azimuthal mode 2 in the jet's far-field regions.

The results and discussion presented here build on the original benchmark studies of Ukeiley, Seiner & Ponton (1999) for the Mach 0.85 compressible shear layer in order to develop a framework for characterizing the low-dimensional features of the turbulent axisymmetric jet as it pertains to acoustic sources of noise. There have been a number of experimental studies of the high subsonic-Mach-number jet using a variety of instruments and jet exit conditions (Morris 1976; Lau, Morris & Fisher 1979; Stromberg, McLaughlin & Trout 1980; Narayanan, Barber & Polak 2002; Arakeri *et al.* 2003; Bridges 2006; Alkislar, Krothapalli & Butler 2007; Iqbal & Thomas 2007), which have been used to guide the current experiments and provide some confidence in the data presented here for discussion. The results that are obtained from this analysis are used in a subsequent discussion (Part 2, Tinney, Ukeiley & Glauser 2008) whereby a low-dimensional model estimate of the most energetic flow events is constructed, from which an analogy with the far-field acoustics is invoked.

The outline of this paper is as follows. A description of the experiment and of the jet exit conditions will be presented in § 2, including an analysis aimed at quantifying the accuracy of the measurements, as well as potential sources of error. In § 3, the spatial evolution of the Fourier-azimuthal modes of the Mach 0.85 axisymmetric jet will be presented followed by an optimization of the radial distribution of the Fourier-modes using proper orthogonal decomposition in § 4. The POD is applied using both scalar and vector forms of the technique, from which the results are compared with what is available in the literature. This is performed to improve our confidence with the measurements reported here under more difficult flow conditions. A low-dimensional reconstruction of the frozen jet structure is performed in § 5 using only the most energetic flow features, followed by a summary in § 6.

2. Experimental description

2.1. *Facility*

The measurements reported here were acquired at Syracuse University's fully anechoic chamber (206 m^3) located on the Skytop campus. Specific details regarding the design and construction of the facility can be found in Dosanjh, Bhutiani & Ahuja (1977) and Tinney *et al.* (2004), whereas only the highlights will be presented here. The facility is designed as a blow-down system whereby a two-stage compressor supplies dry compressed air (−40°C dewpoint) to five large storage tanks (32 m^3 total). A pneumatically actuated valve (via Programmable Logic Control [PLC]) regulates the airflow through the piping system to the jet rig located in the chamber. The jet rig comprises a converging nozzle with an exit diameter of $D = 50.8$ mm. Input to the PLC comprises a Pressure Systems 0.05 % of full scale (FS), 0–25 p.s.i.g. transducer (for sampling the static pressure before the nozzle contraction) and a Transmetrics 26–32 in Hg, 2.5 %FS barometric transducer (for sampling the absolute pressure in the chamber, P_b). The set point for the exit Mach number is monitored using the isentropic, compressible flow relation,

$$M = \left[\frac{2}{\gamma - 1}\left\{\left(\frac{G_p P_s + P_b}{P_b}\right)\gamma - 1/\gamma - 1\right\}\right]^{1/2}, \tag{2.1}$$

where a coefficient ($G_p = P_o/P_s$) has been inserted in place of the pipe's total pressure based on *a priori* calibration of the jet's total pressure (P_o) from the static pressure (P_s). Derivation of the uncertainty propagation equation yields a flow uncertainty (ϵ_M) to within 0.12 % at Mach 0.85 (see Tinney *et al.* 2004).

The air system is designed to operate at a steady jet exit speed of Mach 0.85 for approximately 20 min. The facility is equipped with an electric circulation heater, capable of elevating the jet exit temperatures up to 810°K at Mach 0.85. The measurements presented here will comprise an unheated jet with a centreline exit velocity U_j corresponding to a nominal Mach number of 0.85 ($Re_D = 1 \times 10^6$), exiting into an environment with ambient temperatures around 283°K.

2.2. *Instrumentation*

The primary instrument employed in this investigation for analysis of the jet's mean and turbulent statistics comprised a Dantec Dynamics stereo (three-component) particle image velocimetry (PIV) system. The system's characteristics included two HiSense 12-bit resolution CCD cameras (1280 × 1024 pixels) as well as a New Wave Research 200 mJ Nd:YAG dual head laser (Gemini-PIV) for generating the optical laser sheet ($\lambda_L = 532$ nm). Both cameras comprised square pixels with a lineal dimension of 6.7 μm, 28 mm f/2.8D AF Nikkor ($f^{\#} = 2.8$) lenses and were oriented at 45° to the illumination plane of the laser. The positioning of the PIV system (figure 1) allowed for surveys of the jet's (r, θ)-plane at discrete streamwise locations between $x/D = 3.0$ and 8.0 ($\Delta x/D = 0.25$).

The entire system was mounted on a traverse that provided precise controlled movements (±6.25 μm) of the PIV system without multiple calibrations. At each streamwise position, 1250 image pairs were acquired at a rate of 4 Hz. An estimate of the characteristic time scale of the flow (Tennekes & Lumley 1972) using $T_t \sim D/U_j$ was found to be 1.814×10^{-4} s, suggesting that successive image pairs were statistically independent realizations of the flow. The laser-sheet thickness was 5 mm and the Δt between images, from which the vector maps were calculated, was 4 μs. A Gaussian window was used for calculating the vector maps in order

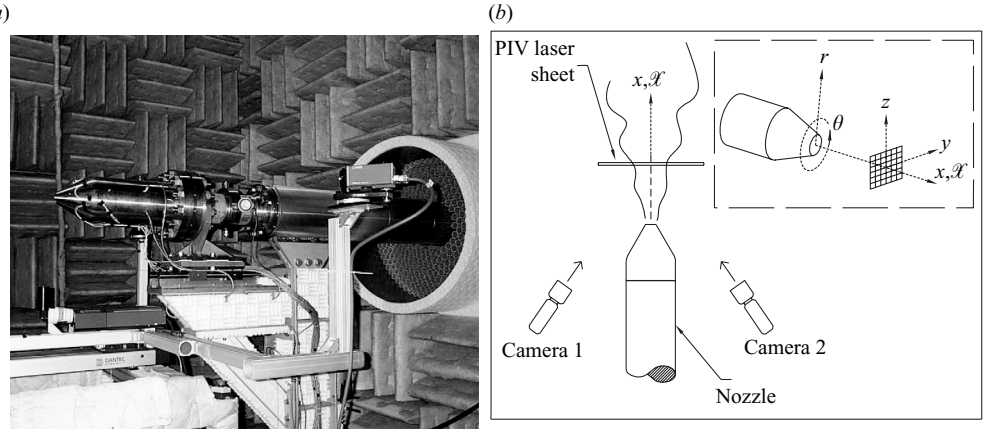

FIGURE 1. (*a*) Experimental arrangement and (*b*) coordinate system.

to reduce phantom correlations while a parabolic sub-pixel interpolation scheme improved the centre of the peak correlation. Since window offsets have been shown by Westerweel, Dabiri & Gharib (1997) to improve the accuracy of the displacement cross-correlation peak, the cross-correlation analysis was performed using the adaptive correlation techniques from Dantec Dynamics' FlowManager software (v3.3) (http://www.dantecdynamics.com) whereby the final interrogation area (16×16 pixels) resulted from three refinement steps that were first initiated using a larger 32×32 pixel interrogation area. This final interrogation area was chosen to improve the signal-to-noise ratio since high gradient flows are known to increase the level of noise relative to the peak signal. Vector maps were generated using a 50 % overlap yielding a Cartesian grid density (after masking to 552×840 pixels) of 69(y) by 101(z) with Cartesian grid spacings of $\Delta y = 2.56\,\text{mm}$ ($5.0 \times 10^{-2} D$) and $\Delta z = 1.68\,\text{mm}$ ($3.3 \times 10^{-2} D$). The small percentage of outlier vectors were replaced by the FlowManager software, and were found mostly in the outer regions of the PIV window. Specific details regarding the transformation of image pairs to vector maps are described in Tinney (2005) following the discussions of Willert & Gharib (1991), Keane & Adrian (1992) and Raffel, Willert & Kompenhans (1998).

Additional instruments used to quantify the jet's characteristics included a Pitot tube, and a Dantec Dynamics laser doppler anemometer (LDA). The Pitot tube comprised a separate Pressure Systems 0.05 %FS accurate, 0–25 p.s.i.g. transducer and a barometric transducer (shared by the PLC) for sampling the total and ambient pressures, respectively. The LDA system employed a 3 W argon ion laser head, and measurements were performed using backward scattering. Seeder pressure was adjusted to achieve LDA sampling rates of the order of 25 kHz. Processing of the LDA data is described in Hall, Glauser & Tinney (2005) and employed a zero-order substitution algorithm discussed by Adrian & Yao (1986). The notation that has been adopted for discussion follows standard literature where the instantaneous field comprises both mean and turbulence quantities, that is, $\tilde{u}_i = U_i + u_i$ and the subscripts $i = 1, 2, 3$ refer to axial u, radial v and azimuthal w components of velocity, respectively.

2.3. *Seeding and tracking errors*

Seeding for the primary jet was provided by a PIVTEC twelve Laskin nozzle seeder, whereas the co-flow region (necessary for the entrainment flow) was supplied by a TSI

model-9307 oil-droplet generator. Both seeders used olive oil as the seeding medium to produce mean particle sizes of the order of $d_p \simeq 1\,\mu\text{m}$; the oil was injected far upstream from the nozzle exit to ensure sufficient mixing. It is known that tracking errors are introduced because the particles do not follow strictly the motion of the fluid (Agüí & Jiménez 1987; Melling 1997). Following the analysis of Melling (1997), the unsteady motion of a sphere of density ρ_p suspended in a fluid with density ρ_f and kinematic viscosity ν can be written as,

$$\frac{\mathrm{d}\tilde{U}_p}{\mathrm{d}t} = -C(\tilde{U}_p - \tilde{U}_f), \tag{2.2}$$

where the ratio between the particle and fluid densities is large $s = \rho_p/\rho_f \gg 1$, and $\tilde{U}_p$ and $\tilde{U}_f$ are the instantaneous velocities of the particle and fluid, respectively. Inserting an expression for the characteristic frequency: $C = 18 f St^{-2}\,\text{s}^{-1}$ in terms of Stokes resistance: $C_D = 24/Re_p$, and neglecting external forces (centrifugal, gravitational, etc.), an analytical expression for the ratios between the particle and fluid motions is determined,

$$\frac{\langle u_p^2 \rangle}{\langle u_f^2 \rangle} = \left(1 + \frac{f_c}{C}\right)^{-1}. \tag{2.3}$$

Here, the Stokes number $St = d_p(f/\nu)^{0.5}$ represents a characteristic non-dimensional frequency of the particle response and f_c is the turbulence frequency associated with the smallest turbulent eddies (to be discussed shortly). According to Melling (1997), an expression for the Stokes resistance (drag coefficient) should be adjusted on account of transonic flow conditions, $C_D = 24/(Re_p(1 + Kn_p))$ whereby the Knudsen number of the particle $Kn_p = l/d_p$ is determined from the mean free path ($l = 0.06\,\mu\text{m}$) of the gas molecules. In doing so, the expression for the characteristic frequency now becomes,

$$C = \frac{18 f}{(1 + Kn_p) St^2 s}, \tag{2.4}$$

from which (2.3) is re-examined using (2.4). The results of this are shown in figure 2(a) for different particle diameters and is complementary to the findings of Melling (1997). As we can see, the disparity between the particle and fluid velocities increases with both increasing frequency and increasing particle diameter. For the case where $d_p = 1\,\mu\text{m}$, the velocity ratio is illustrated with and without correction for the transonic flow conditions thus demonstrating the slight correction that is obtained by considering the particle Knudsen number. The tracking error, expressed as a percentage,

$$\epsilon_{track} = \left(1 - \frac{\langle u_p^2 \rangle}{\langle u_f^2 \rangle}\right) \times 100\,\%, \tag{2.5}$$

is shown in figure 2(b).

Using an approximation that the turbulent length scale is proportional to $\ell = u^3/\epsilon$, the turbulent time scale can be determined, $\tau = \ell/u$ (Tennekes & Lumley 1972), by the substitution of $\epsilon = 0.044 U_j^3/D(D/x)$ from which we obtain (George, Beuther & Arndt 1984),

$$\tau = \frac{u^2}{\epsilon} = \left(\frac{0.16^2}{0.044}\frac{D}{U_j}\frac{x}{D}\right). \tag{2.6}$$

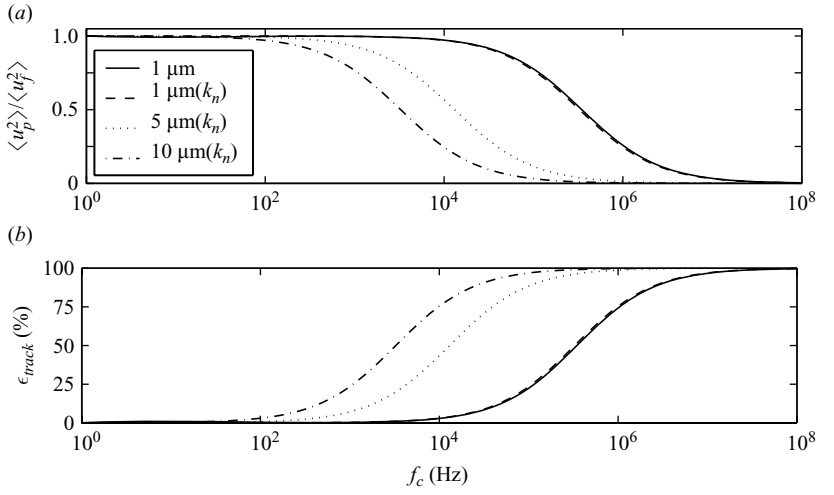

FIGURE 2. (*a*) Particle to fluid velocity ratio for different particle diameters. (*b*) Corresponding tracking error.

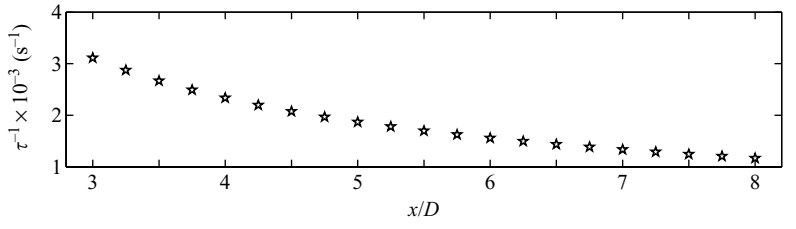

FIGURE 3. Turbulence frequency based on the time scale of the dissipative structure in a Mach 0.85 jet.

This uses an assumption that the ratio between the turbulence and the mean flow is $u/U_j \sim 0.16$ which is shown in § 2.6 to be reasonable. The frequency associated with the dissipative time scale is shown in figure 3 as a function of axial position over which the measurements are performed. Thus, from figure 3, it is clear that the estimate for the turbulence frequency never exceeds 4 kHz, and that tracking errors displayed in figure 2(*b*) are within 0.9 %. The approximation of (2.6) is not dubious for the high-Reynolds-number jet since it is known that the dissipation of turbulent energy is controlled by the energy containing scales of motion.

2.4. *Optical considerations*

For macro PIV systems, the diffraction limited spot-size (Adrian 1991; Westerweel 1998; Raffel *et al.* 1998; Meinhart & Wereley 2003) through a single lens with circular aperture is easily defined,

$$d_s = 2.44(S+1)\lambda_L f^{\#}, \tag{2.7}$$

where S is the average lens magnification and is determined from the calibration to be 0.025. Normally, as we consider the Nyquist sampling criterion, the particle diameter (and optical arrangement) is chosen such that the pixel dimension is less than a quarter of the diffraction limited spot-diameter, i.e. $d_s/d_r \geqslant 4$. However, it has been shown (Westerweel 1998) that error-free estimates of the particle-image centroid can be obtained without satisfying the Nyquist sampling rate since the error is zero when

the cutoff frequency is smaller than $1/d_r$. In this regard, the minimum pixel resolution (d_r) should satisfy $d_s/d_r \geqslant 2$. In the current analysis of the Mach 0.85 jet flow, the ratio d_s/d_r is calculated to be around 0.6. While this is slightly under what was suggested by Westerweel (1998), a slight blurring of the image was incorporated in the PIV measurements which is known to improve the estimate's precision for the particle centroid. Westerweel (1998) has shown that particular care should be taken when blurring images such that the reduction in tracking error is not replaced by increases in random error. Consequently the particle image diameter, $d_\tau = (S^2 d_p^2 + d_s^2)^{0.5}$, was approximated to be 2×10^{-4} m with a particle image displacement of ~ 4 pixels; determined from the centre of the jet where the physical displacement of particles is greatest, and where the turbulence levels are lowest.

2.5. *Grid transformation*

Since the bulk of the analysis of these data was performed in cylindrical coordinates, a transformation of the raw PIV data was necessary, that is, from $y, z, \mathscr{X} \rightarrow r, \theta, x$, where x denotes the streamwise direction in cylindrical coordinates and is shown in figure 1(b). The transformation comprised a triangle-based linear interpolation scheme. The radial increment for the cylindrical grid was calculated using $\Delta r = (\Delta y + \Delta z)/2 = 2.12$ mm, $(4.17 \times 10^{-2} D)$. Likewise, the azimuthal increment was chosen based on where the spatial transformations (used in subsequent discussions) were believed to be most sensitive, that is, towards the centre and low-speed sides of the jet shear layer where the higher modal events are known to exist. This resulted in an azimuthal increment of $\vartheta = 4^\circ$ using a radial separation of $\Delta r = 4.17 \times 10^{-2} D$ at $r/D \sim 0.5$.

To be certain that the coordinate transformation preserved the continuity relation (in a global sense) for the measured data, that is $\partial u_i/\partial x_i = 0$, the spatial derivative of the axial term was computed from the raw data set (in Cartesian coordinates) and compared with the derivative of the axial term in the transformed grid (cylindrical coordinates). Recall that the continuity equation in Cartesian and cylindrical coordinates is, respectively,

$$\frac{\partial u_{\mathscr{X}}}{\partial \mathscr{X}} = -\left(\frac{\partial v_y}{\partial y} + \frac{\partial w_z}{\partial z}\right), \tag{2.8}$$

and

$$\frac{\partial u_x}{\partial x} = -\left(\frac{1}{r}\frac{\partial (r v_r)}{\partial r} + \frac{1}{r}\frac{\partial (w_\theta)}{\partial \theta}\right). \tag{2.9}$$

The following comparison is then made based on the sum of the axial derivatives:

$$\kappa^{car}(\mathscr{X}) = \sum \left|\frac{\partial u_{\mathscr{X}}}{\partial \mathscr{X}}\right|^2, \tag{2.10}$$

$$\kappa^{cyl}(x) = \sum \left|\frac{\partial u_x}{\partial x}\right|^2. \tag{2.11}$$

While $\mathscr{X}$ and x effectively represent identical quantities, they are defined separately in (2.10) and (2.11) to distinguish between the Cartesian (PIV world) and cylindrical coordinates. The derivative was performed using a sixth-order-accurate compact finite-difference scheme. A comparison between $\kappa^{car}(\mathscr{X})$ and $\kappa^{cyl}(x)$ is shown in figure 4 to demonstrate the preservation of the continuity equation after the coordinate

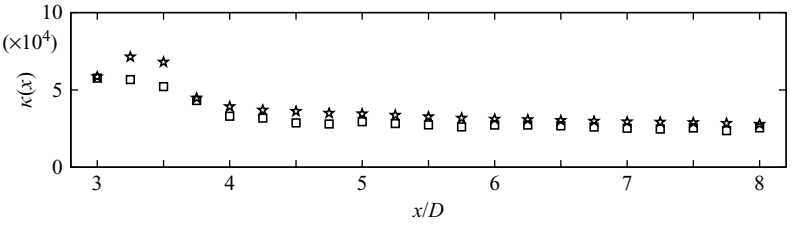

FIGURE 4. Comparison of the bulk solution to the continuity equation between the original (⋆, Cartesian) and transformed (□, cylindrical) grids.

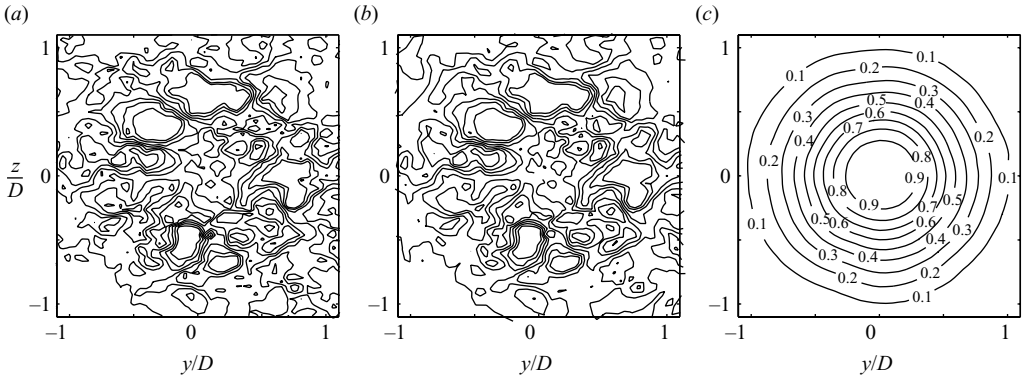

FIGURE 5. Sample snap-shot at $x/D = 5.0$ of the fluctuating streamwise velocity on the (a) Cartesian and (b) cylindrical grids. (c) Mean streamwise velocity ratio at $x/D = 5.0$.

transformation. A maximum difference of 23 % was found at $x/D = 3.5$ which decayed to 12 %–15 % beyond $x/D = 4.0$. These discrepancies were found to be the result of uncorrelated noise in the outer edges of the PIV window (outside of the entrainment region at this axial position) which became amplified by the numerical derivative.

A sample comparison of the transformed fluctuating velocity for a given snap-shot in the flow at $x/D = 5.0$ is shown in figures 5(a) and 5(b), before (original Cartesian grid) and after (new cylindrical grid) the coordinate transformation, respectively. The contour levels for these two figures are identical. The mean streamwise velocity ratio (U/U_j) at $x/D = 5.0$ is also shown (figure 5c) demonstrating the mean axisymmetry of this jet flow.

2.6. *Single-point jet statistics*

Velocity ratios of the jet's axial component are shown in figure 6(a) at $x/D = 0.0$ using the Pitot tube. These are demonstrated for a range of Mach numbers (0.30, 0.60, 0.85) and are complemented with LDA measurements in figure 6(b) at $x/D = 0.50$. We can see that the jet exit profile has a top-hat shape and the initial shear-layer thickness, based on $U = 0.95U_j$ and figure 6(a), was extrapolated from the measured profiles to be $0.0175D$. This is a crude estimate of the shear-layer thickness since the diameter of the Pitot tube's opening is approximately 0.0016 m, or twice the estimated shear-layer thickness. The errors associated with the Pitot tube measurements were discussed by Tinney *et al.* (2004) and were of the order of 0.12 % at Mach 0.85. Axial mean velocity ratios from the PIV measurements are shown in figure 6(c) and are shown to collapse well using the similarity variable: $\eta = (r - r_{0.5})/x$, where x is the downstream distance from the nozzle exit plane and $r_{0.5}$ is the location where

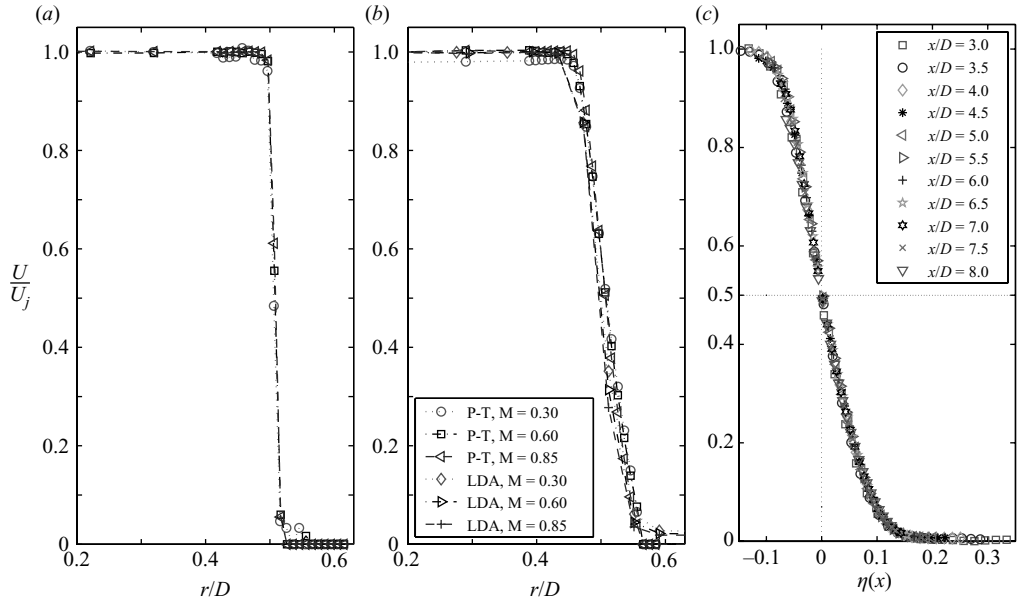

FIGURE 6. Axial mean velocity ratios measured with (*a*) Pitot tube at $x/D = 0$, (*b*) Pitot tube and LDA at $x/D = 0.50$, (*c*) PIV between $x/D = 3.0$ and 8.0.

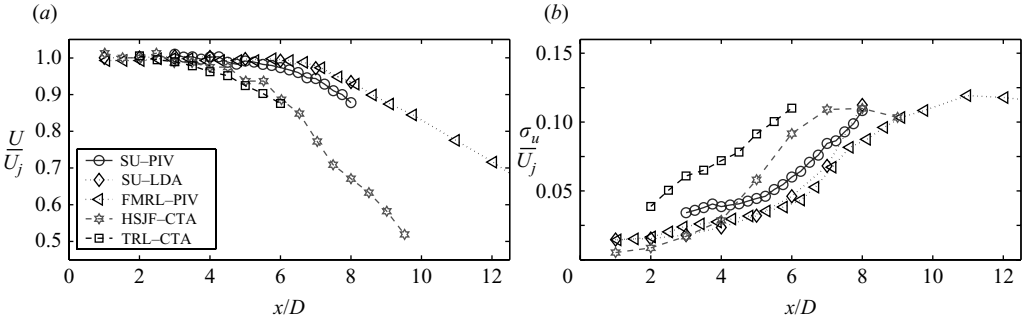

FIGURE 7. Centreline distribution of (*a*) mean velocity U/U_j and (*b*) turbulence intensity σ_u/U_j, from the current Mach 0.85 database compared with other facilities (see table 1).

the mean velocity is 50 % of the jet exit velocity. Turbulence levels from the LDA measurements at the jet's centre and $x/D = 0.5$ were of the order of 1 %. It is plausible that the noise floor of the instrument was reached and so warrants caution when interpreting these turbulence levels as they may be lower than this.

The distribution of the mean (U/U_j) and turbulence (σ_u/U_j) velocity ratios along the centreline are shown in figure 7(*a*, *b*) using the current set of data, alongside the measurements reported from a number of other facilities (table 1). Both profiles from the current data set comprise an inflection point around $x/D = 5.0$, whereas the decay of the mean axial velocity does not reach 95 % of U_j until after $x/D = 6.0$. As expected, the Mach 0.3 measurements of Iqbal & Thomas (2007) decay much earlier than the current Mach 0.85 data, whereas the Mach 0.9 jet measurements of Arakeri *et al.* (2003) and Alkislar *et al.* (2007) occur slightly farther downstream. The turbulence profiles of the Mach 0.3 study in figure 7(*b*) also comprise a more rapid approach into the jet's transitional regions, when compared to the transonic jets

Data source	Mach number	Nozzle diameter mm	Instrument	Facility
Current work	0.85	50.8	PIV/LDA	SU
Alkislar *et al.*(2007)	0.9	69.85	PIV	QAF
Arakeri *et al.* (2003)	0.9	22.2	PIV	FMRL
Iqbal & Thomas (2007)	0.3	50.6	CTA	HSJF
Jung, Gammard & George (2004)	0.07	98	CTA	TRL

TABLE 1. Description of experimental jet measurements reported by others.

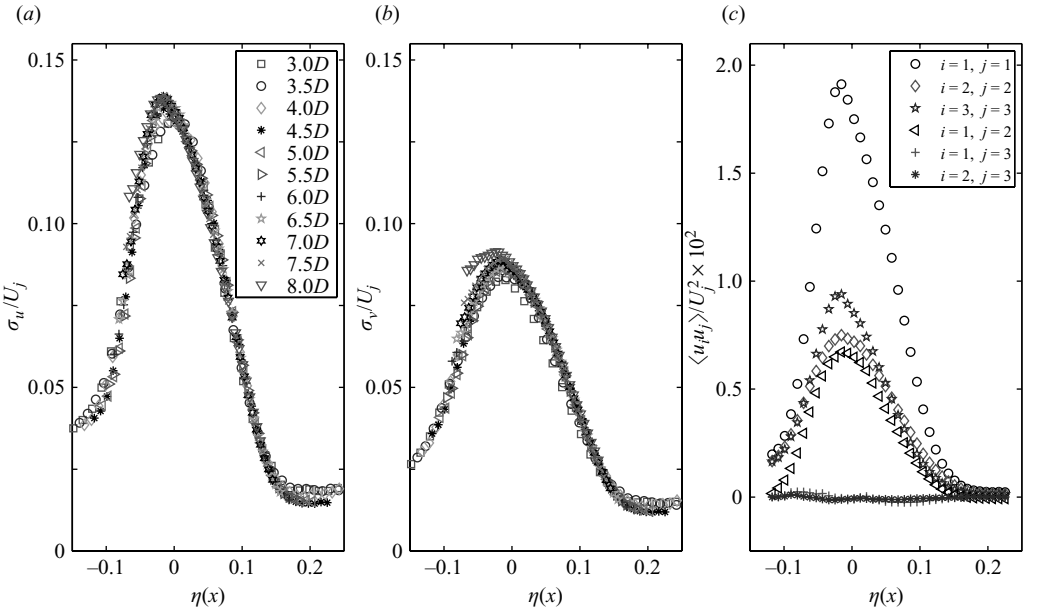

FIGURE 8. Turbulence velocity ratios of the (*a*) axial and (*b*) radial components between $x/D = 3.0$ and 8.0. (*c*) Normal and shear stress terms at $x/D = 5.0$.

(Mach 0.85 and 0.9), the latter of which is a well-known consequence of the lengthier potential core.

Second central moments (σ_i) for all three components of velocity were calculated from the PIV measurements from which the axial and radial components are shown in figure 8(a, b). A sample of all normal and shear stress components are shown in figure 8(c) at $x/D = 5.0$ where u_1u_2 is the only significant non-zero shear stress term (this is only the case when $\vartheta = 0$). The collapse of the mean and turbulence statistics in figures 6(c) and 8(a, b, c) are consistent with the low-speed jet studies of Bradshaw, Ferriss & Johnson (1964), Hussain & Clark (1981) and Jung *et al.* (2004), and the supersonic jet study of Kerhervé *et al.* (2004). Note that the collapse of these profiles continues beyond the end of the potential core, even at $x/D = 8.0$, as was shown by Lau *et al.* (1979) and Jung *et al.* (2004).

Peak turbulence intensities are shown in figure 9, alongside the measurements reported by others. In figure 9(a), the axial component, with a peak around 14 % of the jet exit velocity, demonstrates an acute similarity to the measurements

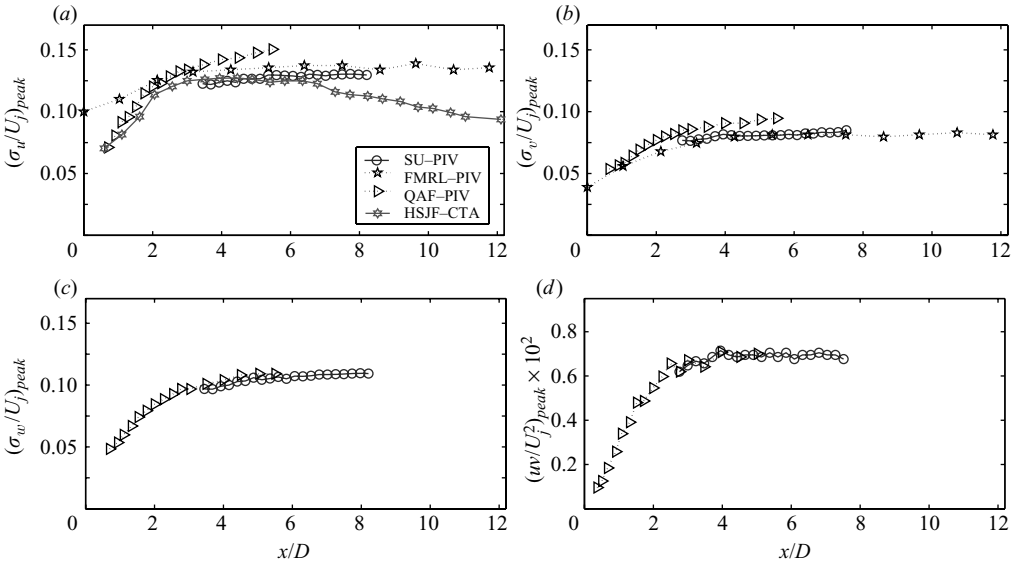

FIGURE 9. Peak turbulence intensities (σ_i/U_j) in the downstream direction compared with other facilities for the (*a*) axial, (*b*) radial and (*c*) azimuthal velocity components. (*d*) The peak shear stress uv/U_j^2.

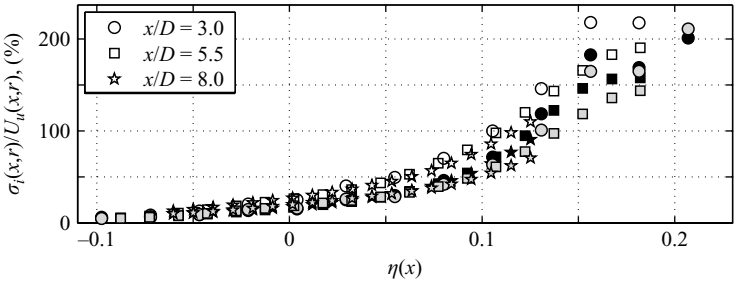

FIGURE 10. Local turbulence intensities: open symbols, u; closed symbols, v; grey symbols, w.

reported by Arakeri *et al.* (2003) and Iqbal & Thomas (2007), the measurements of Alkislar *et al.* (2007) being slightly larger in amplitude. Likewise, the radial and azimuthal turbulence intensities from the current data set exhibit peak energies of the order of 9 % and 10 %, respectively, with a tendency to increase only slightly with increasing x. Similar trends are manifest in the radial and azimuthal components when compared to the reported transonic flow measurements of others. Two-component LDA measurements performed at Mach 0.85 in the current facility resulted in peak turbulence levels of σ_u and σ_v of 15 % and 11 %, respectively. Thus, a small filtering effect is evident with the PIV measurements when compared to CTA and LDA instruments.

As the PIV system allows for a more accurate assessment of the low-speed entrainment regions of the flow, the local turbulence intensities are calculated at three axial positions and are shown in figure 10. The profiles demonstrate the significant increases in turbulence levels in the low-speed regions of the flow; shown here to be well above 50 % when $\eta(x) > 0.1$.

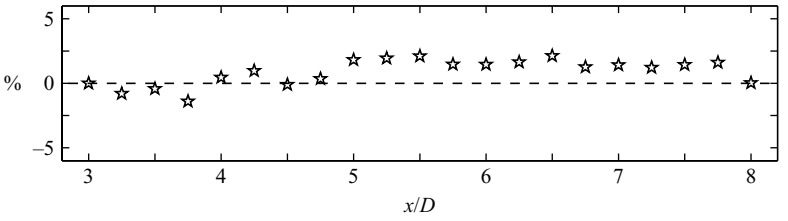

FIGURE 11. Percentage variation of the momentum integral.

2.7. *Momentum integral*

In order to determine whether the experimental data satisfy the equations believed to govern the flow, and that the data give in fact a reasonable model of an axisymmetric jet in an infinite environment according to Hussein, Capp & George (1994), then the velocity moment profiles should satisfy the momentum integral given to the second order,

$$M_o = 2\pi \int_0^\infty [U^2 + \langle u^2 \rangle - \tfrac{1}{2}(\langle v^2 \rangle + \langle w^2 \rangle)] r \, \mathrm{d}r. \tag{2.12}$$

The percentage variation of (2.12), expressed as,

$$\frac{M_o(x) - M_o(3)}{M_o(3)} \times 100 \tag{2.13}$$

is shown in figure 11 using the PIV measurements to demonstrate the variation of the momentum integral (less than 5 %) throughout the range of positions studied.

Sample snap-shots from the PIV measurements are shown in figure 12 at three axial stations in the flow, demonstrating the resolution that the PIV system affords and the coherent large-scale behaviour of the Mach 0.85 jet. At $x/D = 3.0$ in figure 12(a), we can see the presence of the irrotational potential core region and evidence of counter-rotating structures in the shear layer; whereas at $x/D = 5.0$, the potential core has shrunk, the consequence of larger events in the shear layer. By $x/D = 7.0$, the coherent large-scale motions are seen here to have completely engulfed the potential core.

2.8. *Far-field pressure*

Pressure measurements in the acoustic far-field regions of the jet flow at $r/D = 75$ were performed using an arc array of six G.R.A.S type–*40BE* 1/4 inch pre-polarized free-field condenser microphones with matching preamplifiers (see Tinney *et al.* 2004, for details regarding these acoustic measurements). The arrangement of these instruments relative to the jet axis are shown in figure 13(a). The power spectral density, generated from an ensemble average of 375 blocks of 2^{13} samples per block (sampled at 75 kHz) are shown in figure 13(b) using $\delta f = 9.16$ Hz. No corrections for atmospheric attenuation have been performed, though a 10 % bandwidth moving filter has been used to smooth the spectra. The non-dimensional frequency is defined by $St_D = fDU_j^{-1}$. As can be seen in figure 13(b), shallow angles to the jet axis are dominated by low frequencies ($St_D = 0.15$) whereas angles perpendicular to the flow (90°) are dominated by high frequencies ($St_D = 0.3$). The OASPL directivity is also shown in figure 14 and compares well with the far-field acoustic measurements of a Mach 0.9 jet by Alkislar *et al.* (2007). While the principal discussion is focused on characterizing the low-dimensional behaviour of the near-field velocity, the acoustic

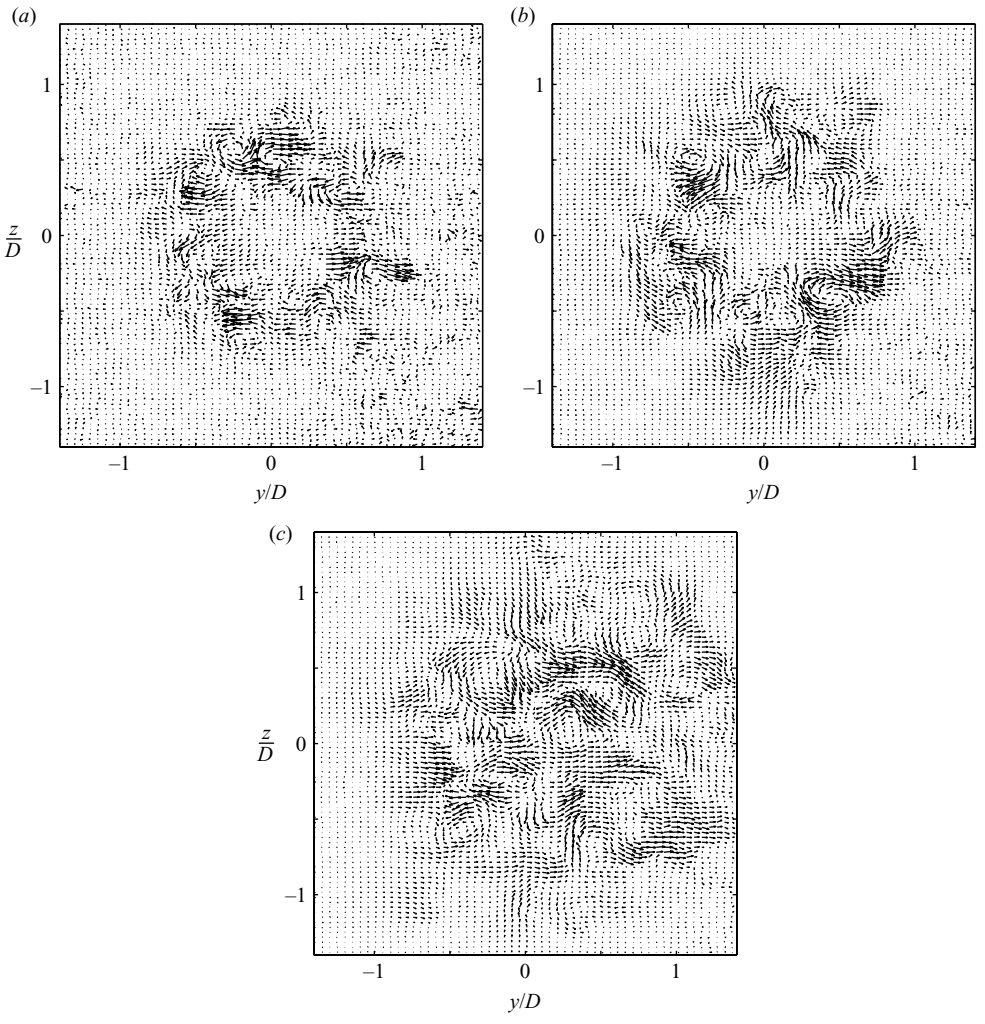

FIGURE 12. PIV snap-shots of the streamwise normal component velocities in the (y, z)-plane of the jet. (a) $x/D = 3.0$, (b) 5.0, (c) 7.0.

far-field measurements are here presented to provide a more complete picture of this Mach 0.85 jet. These far-field measurements will be important in Part 2 where a prediction of the far-field pressure at these observer points is obtained using a three-dimensional, three-component, low-dimensional estimate of this jet flow.

3. Two-point statistics: Fourier-azimuthal features of the jet

Because of the nature of planar optical measurements via stereo PIV, all three components of the velocity field were captured across the (r, θ)-plane of the jet, from which the spatial distribution of all nine normal and shear stress terms were calculated as follows,

$$R_{ij}(r, r', x, \vartheta) = \langle u_i(r, x, \theta, t) u_j(r', x, \theta + \vartheta, t) \rangle. \tag{3.1}$$

Here, ϑ denotes an azimuthal spatial separation of 4°. See Ukeiley *et al.* (2007) for a discussion regarding the spatial characteristics of the two-point correlations calculated

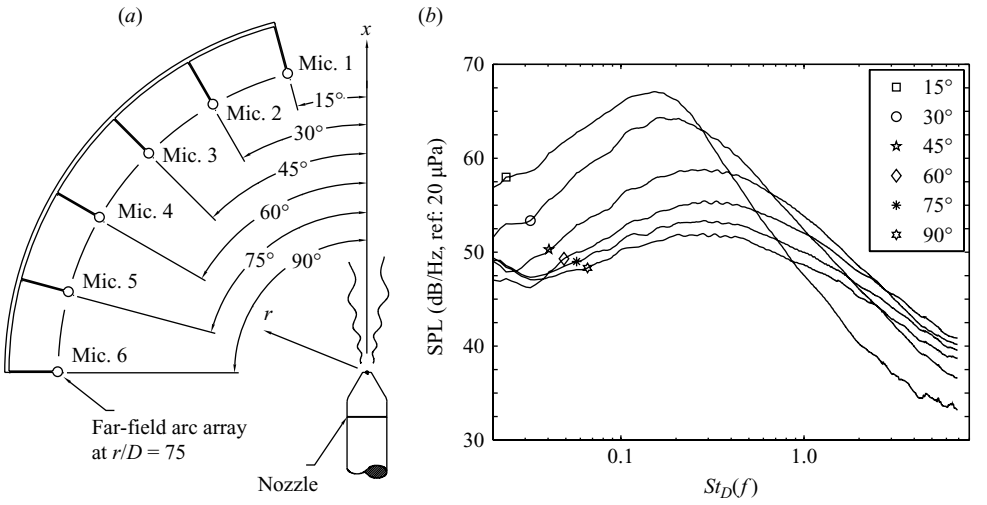

FIGURE 13. (*a*) Experimental arrangement of far-field pressure array. (*b*) Pressure power spectral density at $r/D = 75$.

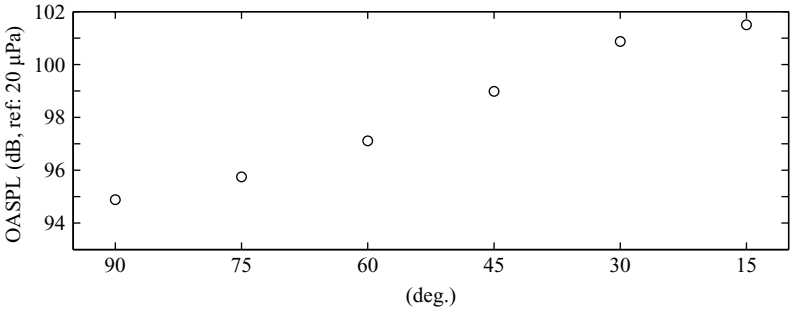

FIGURE 14. OASPL directivity at $r/D = 75$.

from this data set. Since it has been shown that the mean and turbulence statistics of axisymmetric flows are invariant to the origin in azimuth (Glauser 1987; Citriniti & George 2000; Tinney *et al.* 2006*b*), it is quite natural to obtain Fourier-azimuthal modes from the azimuthal two-point statistics,

$$B_{ij}(r, r', x; m) = \frac{1}{2\pi} \int_{-\pi}^{\pi} R_{ij}(r, r', x, \vartheta)\, \mathrm{e}^{-\mathrm{i}m\vartheta}\, \mathrm{d}\vartheta. \tag{3.2}$$

Although it has been suggested that a cosine transformation sufficiently represents the Fourier-azimuthal features of axisymmetric flows, the assumption has been made in an effort to reduce the complexity of the experiment (see Glauser 1987; Tinney *et al.* 2006*b*; Iqbal & Thomas 2007), especially when CTA tools are employed (similar assumptions were made by Moin & Moser (1989) to increase the statistical sample size for the turbulence in a channel). The instrument that has been selected for this investigation of the axisymmetric shear layer provides an opportunity to check this assumption in accordance with the concerns raised by Jung *et al.* (2004) and Wänström, George & Meyer (2006). Keeping in mind that the uncertainties associated with experimental tools will always unavoidably affect our ability to produce 'truly' symmetric statistical quantities, wherever they may exist. Therefore

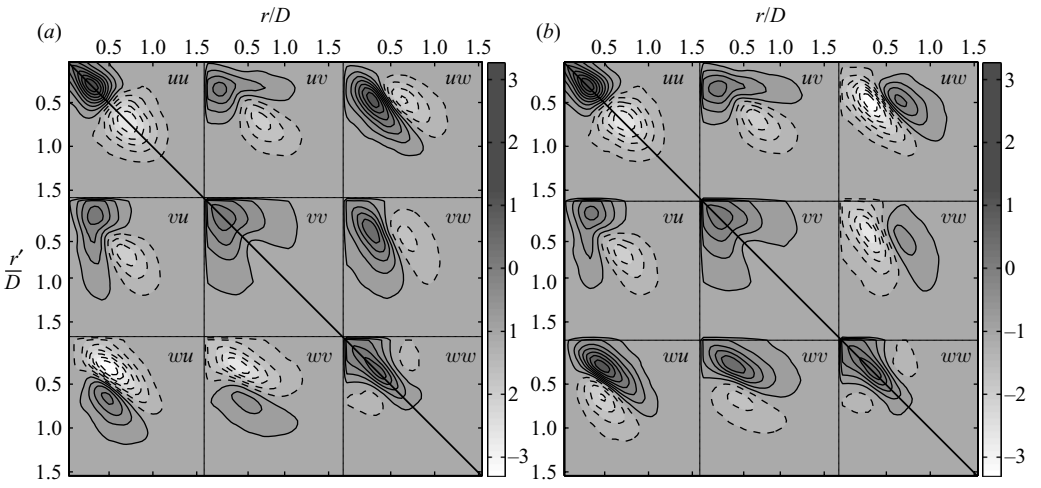

FIGURE 15. The full kernel matrix $R_{ij}(r, r', \vartheta; x) \times 10^3/U_{cl}^2$ at $x/D = 5.0$ with (a) $+\vartheta$ and (b) $-\vartheta$ azimuthal separations of 28°.

it is important to identify the relative magnitude of such asymmetries in order to determine whether it is a consequence of the instrument's accuracy, or a natural artefact of the flow. A sample of the full two-point Reynolds-stress matrix (time suppressed with zero-time lag) comprising all nine normal and shear terms is shown in figure 15 from the measurements at $x/D = 5.0$. These spatial correlations are constructed using (3.1) with $+\vartheta$ (figure 15a) and $-\vartheta$ (figure 15b) azimuthal separations arbitrarily chosen to be 28°. The abscissa and ordinate axis represent repeated spatial positions of r/D and r'/D, respectively, from 0 to 1.5, while a line has been drawn identifying the axis of symmetry with negative contours outlined with dashed lines. Close observation shows that all of the normal stresses (uu, vv, ww) are symmetric about $r = r'$ within the statistical uncertainty of the measurements and that the streamwise-radial shear stress (uv) reflects the transpose of its counterpart (vu) which is also shown to be invariant to positive and negative separations in azimuth. Therefore, the following equalities are representative of these particular terms in the flow:

$$R_{uv}(r, r', +\vartheta) = R_{vu}(r', r, +\vartheta) = R_{uv}(r, r', -\vartheta) = R_{vu}(r', r, -\vartheta), \tag{3.3}$$

thus justifying the assumptions made by Glauser (1987) who measured the jet's uv components of velocity and hence used a symmetry assumption to reduce the number of azimuthal spatial points by a factor of two.

The azimuthal shear-stress terms (uw, vw, wv, wu), however, demonstrate drastically different features relative to the former stress terms (uu, vv, ww, uv, vu). Foremost, these shear-stress terms are clearly non-zero for non-zero azimuthal separations, unlike the r.m.s. profiles in figure 8(c) where, of course, $\vartheta = 0°$. Furthermore, contrary to the observations of uv and vu, the azimuthal shear stresses are shown to satisfy a clearly unique relation, where $i, j = 2, 3$ and $i \neq j$,

$$R_{ij}(r, r', -\vartheta) = R_{ji}(r', r, \vartheta) = -R_{ji}(r', r, -\vartheta). \tag{3.4}$$

Whence, the Fourier-azimuthal series transformation of all of the normal stresses (uu, vv, ww) and the streamwise-radial shear stresses (uv, vu) are shown here to satisfy the condition for the even cosine transformation, whereas the azimuthal shear stresses

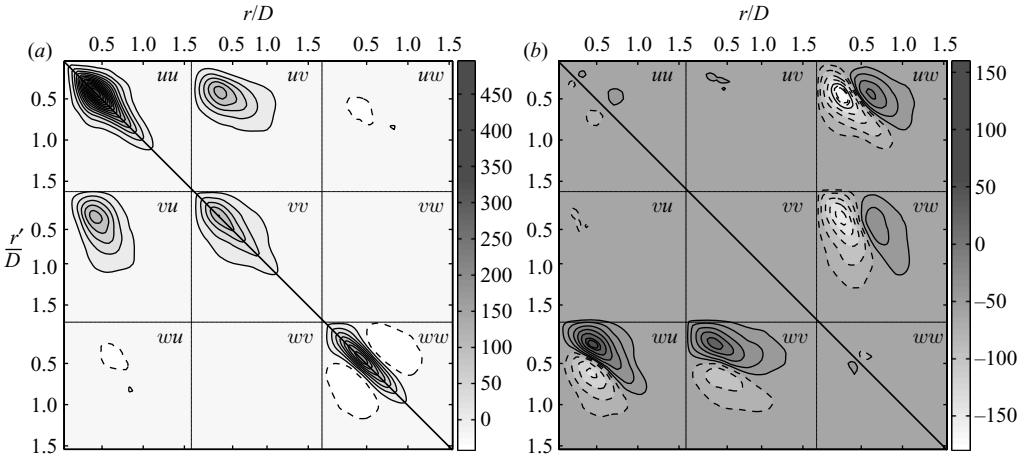

FIGURE 16. (*a*) Real and (*b*) imaginary components of Fourier-azimuthal mode 3 for the full kernel matrix at $x/D = 5.0$.

(uw, vw, wv, wu) satisfy the condition for the odd sine transformation. To further demonstrate these observations, the full Reynolds-stress matrix in figure 15 has been transformed using (3.2) from which both the real and imaginary parts of the Fourier-series coefficients are preserved and are shown in figure 16, using azimuthal mode 3 as an example. As expected, the real part of the coefficients comprise all of the normal (uu, vv, ww) and streamwise-radial (uv, vu) shear-stress terms, while the shear-stress terms associated with the azimuthal velocity component (uw, vw, wv, wu) manifest the imaginary part of the Fourier-series coefficients. The odd sine transformation is a consequence of counter-rotating structures in the shear-layer regions of the jet flow (see figure 12). The jet shear layer is therefore shown here to be a reflection of the following generalization of the Fourier-azimuthal coefficients for all nine Reynolds-stress terms,

$$B_{ij}(r, r'; -m) = B_{ji}(r', r; m) = B^*_{ij}(r, r'; m), \tag{3.5}$$

and is truly Hermitian symmetric.

A further discussion is necessary as we concern ourselves with the spatial topology of these two-point correlations, and their Fourier-azimuthal features. In view of the normal stresses, the azimuthal component of velocity is the only component whose cross-diagonal terms are negative, while the axial and radial components asymptote towards zero. Thus, the azimuthal component is the only velocity component whose fluctuations are opposite in direction with respect to the high- and low-speed sides of the shear layer. This goes to show the high level of axial vorticity that is present in this transonic, high-Reynolds-number jet flow and is significant to the convergence of the POD eigenvalues as will be discussed in § 4.

The complex modulus of the Fourier-azimuthal transformation of all three normal stress components of the kernel (B_{ii}) are shown as surface contours in figure 17 to provide a basic understanding of the radial distributions of the azimuthal modal energy of the axisymmetric jet. In each plot, the distributions of the azimuthal modes are normalized by the energy of the half spectrum for each individual stress term and each axial position in the flow. The axial positions are chosen to illustrate the spatial distribution of these modes before $(3.0D)$, during $(5.0D)$ and after $(7.0D)$ the collapse of the potential core. The decrement for each contour line is 0.2, and the

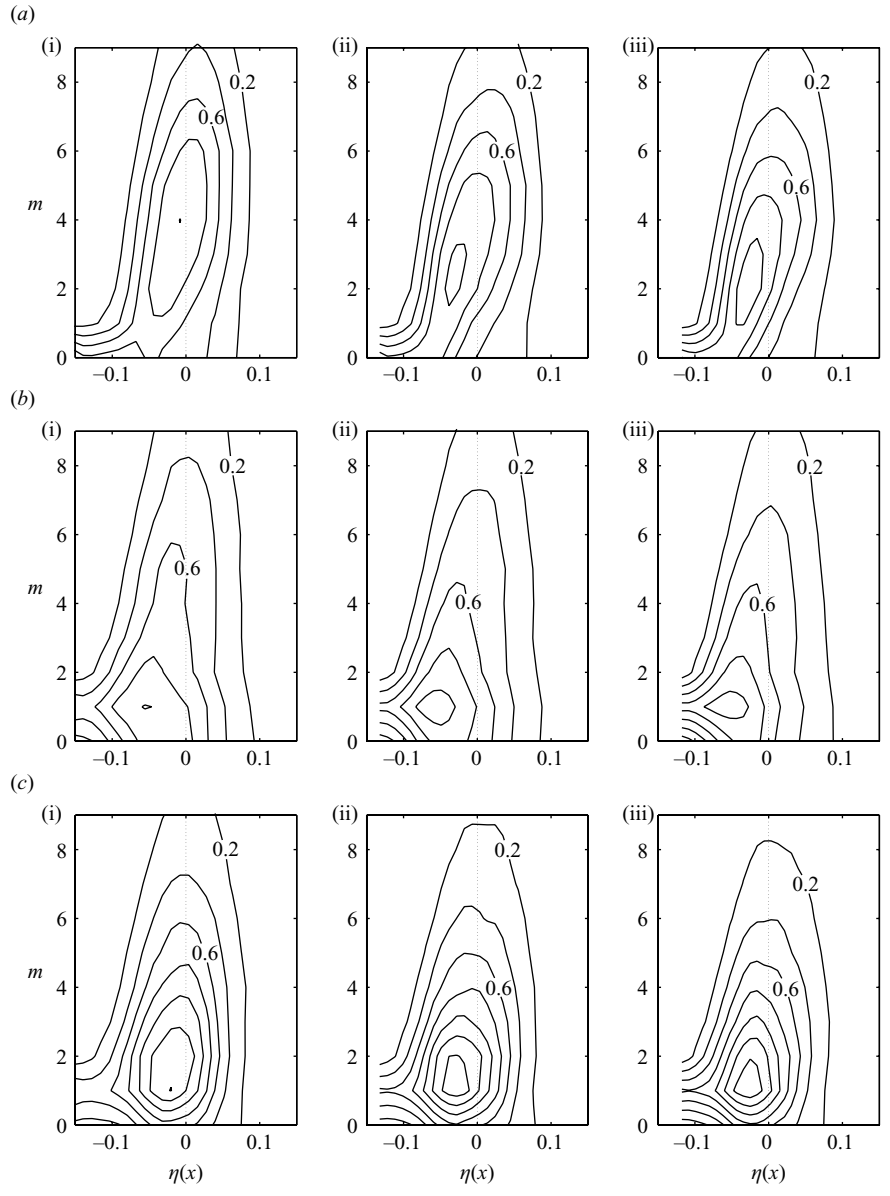

FIGURE 17. Fourier-azimuthal modal distribution of the (*a*) axial, (*b*) radial and (*c*) azimuthal components of velocity. (i) $x/D = 3$, (ii) 5, (iii) 7.

radial distributions of the azimuthal modes are plotted with the similarity variable $\eta(x)$. Prompted by the discussion from Glauser (1987) and Glauser & George (1992), a study of the sensitivity of these solutions to the azimuthal grid spacing (4°) was investigated by Tinney *et al.* (2005) to show that there were negligible spatial aliasing effects. It can be seen in figure 17(*a*) that the axial component of velocity is dominated by $m = 4$ along the centre of the jet's mixing layer at $x/D = 3.0$ and falls to Fourier-azimuthal mode 2 at $x/D = 7.0$ with its peak occurring along the high-speed side of the jet's shear layer. Where the potential core regions of the flow are concerned, the streamwise component is dominated by $m = 0$ at all axial positions, whereas

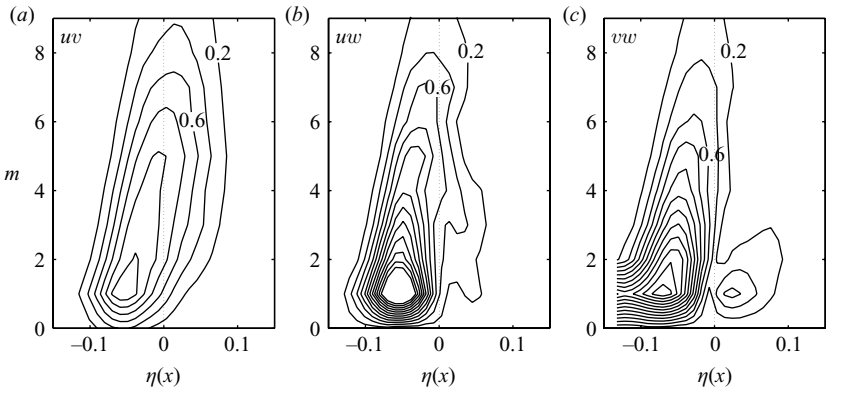

FIGURE 18. Fourier-azimuthal modal distribution of the (*a*) uv, (*b*) uw, and (*c*) vw shear stresses at $x/D = 5.0$.

the radial and azimuthal components comprise the helical $m = 1$ mode (figure 17). Thus the radial and azimuthal component velocities are characterized by more lower-dimensional-flow events, with respect to the axial component. Overall, it is clear that the lower-order modes dominate the potential core and high-speed sides of the jet's mixing layer, whereas the higher-order modes dominate the low-speed side of the jet's mixing layer, in agreement with the observations of Glauser (1987) and Ukeiley *et al.* (1999).

Likewise, the radial distribution of the azimuthal modes of the shear stress terms at $x/D = 5.0$ are shown in figure 18. The uv shear-stress terms in figure 18(a) are shown to assimilate similar features of the axial and radial normal stresses in figure 17(a, b). However, the azimuthal modes of the azimuthal shear stress terms uw and vw in figure 18(b, c), reflect different features to the former. These shear-stress terms show how the modal behaviour on the low-speed side of the shear layer $\eta(x) > 0$ is a close reflection of the azimuthal modes on the high-speed side at $\eta(x) < 0$.

4. Proper orthogonal decomposition

To obtain a low-dimensional representation of the turbulent jet's most energetic flow features, Lumley's (1967) proper orthogonal decomposition (POD) is used to decompose the inhomogeneous radial direction of the flow measurements. While POD reduces to a harmonic decomposition for homogenous, periodic or stationary systems, Fourier methods are much more computationally efficient and so have been used here to treat the azimuthal field prior to the analysis on the radial field using POD. The application of this technique to the current study involving the Mach 0.85 jet comprised both scalar and vector forms of the POD, of which the form of the latter is used to highlight its mathematical features. The general mathematical properties of the POD are described elsewhere (Glauser 1987; Aubry *et al.* 1988; Berkooz *et al.* 1993; Citriniti & George 2000) as a means by which to decompose (in an unbiased manner) inhomogeneous fields comprising spatially correlated events. In short, the POD, derived via the calculus of variations, seeks to maximize the mean square projection of a candidate event onto a field of vectors. The kernel used in the maximization is complex Hermitian, and the problem results in a linear integral equation of the Fredholm type (4.1) following the Hilbert–Schmidt theory

for symmetric integral kernels:

$$\int_R B_{ij}(r, r', x; m)\Phi_j^{(n)}(r', x; m)r'\mathrm{d}r' = \Lambda^{(n)}(x; m)\Phi_i^{(n)}(r, x; m). \tag{4.1}$$

Here the kernel $B_{ij}(r, r', x; m)$ is the ensemble-averaged Fourier-transformed ($\vartheta \rightarrow m$) two-point velocity cross-correlation tensor from (3.2) and r' is the Jacobian for the cylindrical coordinate system and is inside the integral. The solution to the POD produces an ordered sequence of eigenvalues ($\lambda^{(n)} \geqslant \lambda^{(n+1)}$), whose eigenfunctions represent more fluctuating energy per mode than any other linear expansion technique. Although an infinite number of solutions are known to exist, they are limited in practice to the number of points (N) measured multiplied by the number of components (c) used to construct the kernel. Since the eigenvalues and eigenfunctions are properties of the kernel, they can be used to reconstruct it as follows:

$$\mathscr{B}_{ij}^{(k)}(r, r', x; m) = \sum_{n=1}^{k} \lambda^{(n)}(x; m)\Phi_i^{(n)}(r, x; m)\Phi_j^{(n)*}(r', x; m), \tag{4.2}$$

where $\mathscr{B}_{ij}^{(k)}(r, r', x; m) = B_{ij}(r, r', x; m)$ for $k = cN$, and $(^*)$ denotes the complex conjugate. Likewise, an infinite number of eigenfunctions can be used to reconstruct the original instantaneous velocity,

$$u_i(r, x, t; m) = \sum_{n=1}^{k} a^{(n)}(x, t; m)\Phi_i^{(n)}(r, x; m), \tag{4.3}$$

using random and uncorrelated expansion coefficients,

$$a^{(n)}(x, t; m) = \int_R u_i(r, x, t; m)\Phi_i^{(n)*}(r, x; m)r\,\mathrm{d}r, \tag{4.4}$$

whose mean square energies are the eigenvalues themselves: $\Lambda^{(n)} = \langle a^{(n)}a^{(q)}\rangle\delta_{(n,q)}$.

A numerical approximation of the integral is performed using a quadrature function and is achieved by first separating r' into $r'^{1/2} \times r'^{1/2}$, and then multiplying (4.1) by $r^{1/2}$. The kernel is then redefined as $r^{1/2}B_{ij}(r, r', x; m)r'^{1/2}$ from which the empirical basis functions then become $\Phi^{(n)}(r, x; m)r^{1/2}$. The results of this operation ensure that the kernel is Hermitian symmetric without affecting the final solution, and has been shown by Glauser (1987) and Citriniti & George (2000) to simplify the computation.

Where the scalar form of the POD is concerned, its implementation in the current study comprised individual decompositions of the axial–, radial– and azimuthal–normal stresses and is given by the solution to the following integral eigenvalue problem,

$$\int_R B_{ii}(r, r', x; m)\phi_i^{(n)}(r', x; m)r'\mathrm{d}r' = \lambda_i^{(n)}(x; m)\phi_i^{(n)}(r, x; m). \tag{4.5}$$

Since the scalar form of the technique contains all of the same mathematical features as the vector form, it is unnecessary to provide a complete description of both. However, it is provided in (4.5) to form a nomenclature from which the results from the scalar and vector methods can be distinguished in the subsequent discussion. Thus, where appropriate, we will resort to upper and lower case lettering, e.g. (Φ, Λ) versus (ϕ, λ), for those terms that relate to the vector and scalar techniques, respectively.

Although it is customary to use the snap-shot methods of Sirovich (1987) when data sets comprising high spatial resolution are employed – such as those acquired with PIV

Component	$n=1$	$n=2$	$n=3$	$n=4$	$n=5$
$\xi^{(n)}_{u,full}$	46.5	19.8 (66.3)	10.8 (77.1)	6.5 (83.6)	4.2 (87.8)
$\xi^{(n)}_{v,full}$	47.0	19.8 (66.8)	10.6 (77.4)	6.4 (83.8)	4.1 (87.9)
$\xi^{(n)}_{w,full}$	31.4	26.3 (57.7)	13.2 (70.9)	8.9 (79.8)	5.4 (85.2)
$\Xi^{(n)}_{full}$	33.5	15.5 (49.0)	8.2 (57.2)	5.2 (62.4)	4.6 (67.0)

TABLE 2. Percentage contribution of energy in the first five POD modes (averaged in x) including their cumulative convergence in parentheses.

techniques (see Caraballo *et al.* 2003) or in the numerical modelling communities (see Noack, Papas & Monkewitz 2005) – the purpose of treating the azimuthal and radial directions separately is to take advantage of the flow's azimuthal symmetries. Thus, for the remainder of the discussion, we will treat the POD modes as a mean square optimization of the radial distribution of the Fourier-azimuthal modes.

4.1. *Energy convergence and sensitivity*

Since the POD is a decomposition of energy, the cumulative energy is equal to the total resolved turbulent kinetic energy of the flow (Lumley 1967). This is calculated at each axial station as follows:

$$\zeta_i(x) = \sum_n \sum_m \lambda_i^{(n)}(x;m), \tag{4.6}$$

$$\Pi(x) = \sum_n \sum_m \Lambda^{(n)}(x;m). \tag{4.7}$$

It is typical to illustrate the convergence of the POD eigenfunctions in order to determine how the energy-containing events are ranked; calculated here at each axial position by the following energy normalization,

$$\xi^{(n)}_{i,full}(x) = \frac{\sum_m \lambda_i^{(n)}(x;m)}{\zeta_i(x)}, \tag{4.8}$$

$$\Xi^{(n)}_{full}(x) = \frac{\sum_m \Lambda^{(n)}(x;m)}{\Pi(x)}. \tag{4.9}$$

The subscript '*full*' in (4.8) and (4.9) has been inserted and refers to the solutions obtained using the fully resolved measurement grid. The significance of this will be addressed in the subsequent discussion pertaining to the sensitivity of the POD eigenvalues to the resolution of the measurement grid. In table 2, the convergence of the first five POD modes are itemized and were averaged in x since the variation in the normalized energy of the first five POD modes was found to be within 5 % of the averaged normalized values with no observable trends in x. Where the scalar POD eigenvalues are concerned, the axial and radial components exhibit rapid convergence with approximately 77 % of the total energy being resolved in the first three POD modes (8 % of the total number of POD modes). To the contrary, the first two POD eigenvalues of the azimuthal component are shown to possess similar energy levels: 31 % and 26 %, respectively. This pairing-like phenomena is a consequence of the cross-diagonal characteristic of the azimuthal normal stress term discussed in § 3

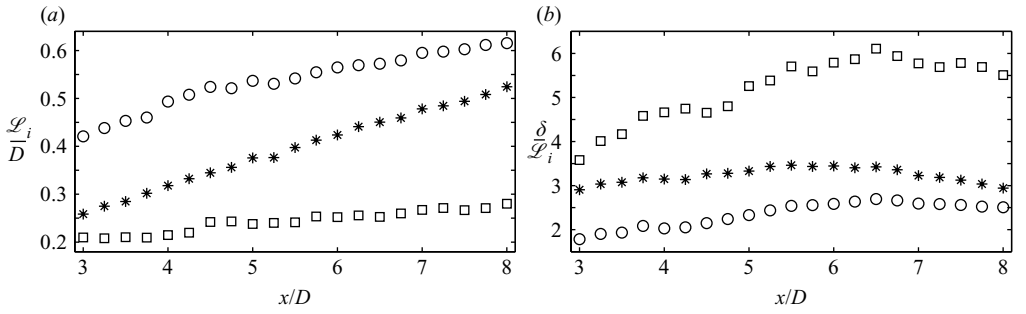

FIGURE 19. (*a*) The Eulerian integral length scales of the flow. (*b*) Ratio between the integral length scales and the shear-layer thickness. *, u; ○, v; □, w.

(axial vorticity) which is shown here to produce a nearly harmonic set of POD basis (POD mode pairs being representative of positive and negative wavenumbers; see Tinney & Jordan 2008).

It is known from Glauser & George (1992) that the spatial resolution of the measurement grid can adversely influence the convergence of the eigenvalues. To demonstrate this effect, a sensitivity study is performed to analyse the convergence of the POD eigenvalues itemized in table 2. In figure 19(*a*), Eulerian integral length scales ($\mathscr{L}_i$) are shown for each component of the velocity field and are calculated as follows:

$$\mathscr{L}_i(x) = \int_r^{r'} \frac{R_{ii}(r, r', x)}{\sigma_i(r, x)\sigma_i(r', x)}\, \mathrm{d}r', \tag{4.10}$$

where $\mathscr{L}_i(x)$ is taken as the maximum value for a given axial location in the flow and was found to reside towards the low-speed regions of the jet shear layer, although similar to the values found along the lip-line at $r/D = 0.5$. The integral length scales are dependent on the component of velocity selected and on the axial position measured. Ratios between the integral length scales and the shear layer's width (δ) are presented in figure 19(*b*); the shear-layer width being defined as the region between $\eta(x) = -0.1$ and 0.17, following the findings reported in figure 8(*c*) and is a sufficient definition for the purposes of this analysis. As the growth of δ changes after the collapse of the potential core, the decay in $\delta/\mathscr{L}_i$ after $x/D \sim 6$ is expected. Glauser & George (1992) estimated $\delta/\mathscr{L}_u$ to be between 3 and 5 for the axial velocity and is within the range of numbers reported here.

The sensitivity of the energy in the POD eigenvalues to the discretization of the integral length scale is shown in figure 20 for the scalar POD solutions (4.8). The solutions obtained using the full measurement grid ($\xi^{(n)}_{i,full}(x)$) have been subtracted to determine the amount of bias in the solutions obtained with the under-resolved grid; the dependence on the axial position being preserved here since the 5 % variation in the fully converged solutions is enough to prevent any discernible trends from collapsing. Not surprisingly, a sensitivity to the discretization of the shear layer is observed where the eigenvalues are shown to converge to within 1 % of the expected value when $\Delta r/\mathscr{L}_i < 0.3$; the radial component of velocity appearing to be more sensitive for $\Delta r/\mathscr{L}_v > 0.3$. As POD-based norms comprise finite energy, the over-prediction of energy in the first POD eigenvalue can result in an under-prediction of energy in higher-mode-number eigenvalues. Evidence of this is shown in figure 20(*d*) where the second POD eigenvalue tends towards an under-prediction in energy as

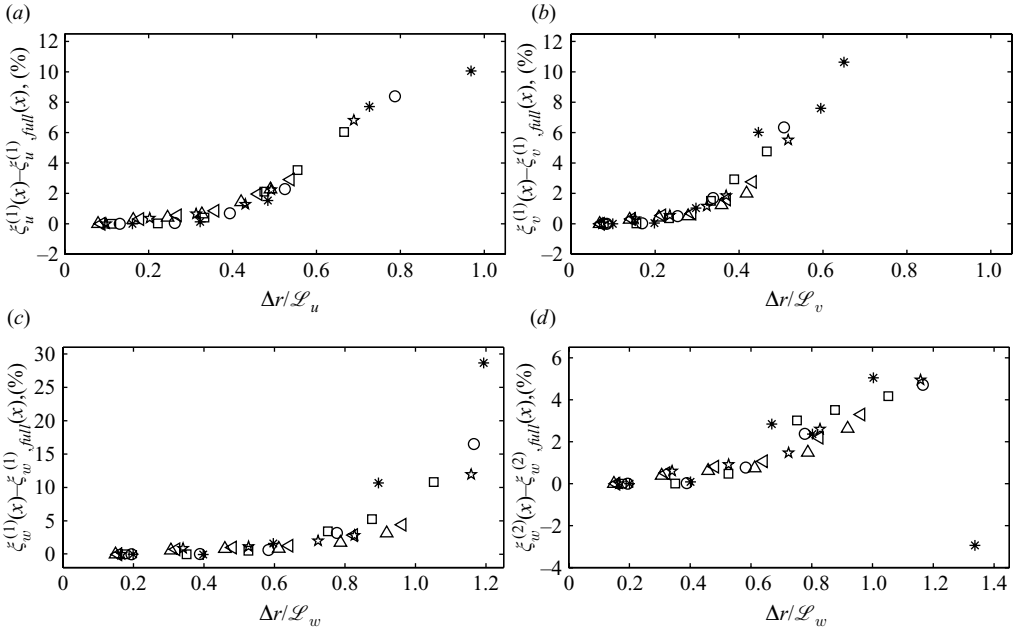

FIGURE 20. Convergence sensitivity of the first POD eigenvalue from the scalar decomposition of the (*a*) axial, (*b*) radial and (*c*) azimuthal components of velocity. (*d*) Convergence sensitivity of the second POD eigenvalue from the scalar decomposition of the azimuthal component. *, $x/D = 3.0$; 0, 4.0; □, 5.0; ⋆, 6.0; △, 7.0; △, 8.0.

the spatial discretization becomes coarser (as Δr exceeds the integral length scale). Similar trends were observed for the vector solutions.

The premise that the eigenvalue energy is proportional to $\delta/\mathscr{L}_i$ is reviewed here and is found to be an important criterion in the axisymmetric jet, and may be equally suitable for other flows. Since an *a priori* estimate of δ may be more readily available, as opposed to $\mathscr{L}_i$, the eigenvalues were found to converge to within 1% of the expected value when $\Delta r/\delta < 0.1$. These trends support the assertions of Glauser & George (1992) that the number of realizations N should be of the order of $1 + 2\delta/\mathscr{L}_i$. For the remainder of this discussion, only those solutions obtained using the fully resolved measurement grid will be used.

4.2. *Fourier-azimuthal eigenspectra*

The normalized Fourier-azimuthal mode eigenspectra are determined from the scalar and vector solutions as follows,

$$\alpha_i^{(n)}(x;m) = \frac{\lambda_i^{(n)}(x;m)}{\zeta_i(x)}, \tag{4.11}$$

$$\beta^{(n)}(x;m) = \frac{\Lambda^{(n)}(x;m)}{\Pi(x)}. \tag{4.12}$$

The distribution of Fourier-azimuthal energy from the scalar decomposition of the axial velocity component is shown in figure 21 using (4.11) and the first three POD modes. As expected, the axial component at $x/D = 3.0$ is rich in higher azimuthal mode number activity which evolves gradually towards lower mode number activity in the transition and far-field regions of the jet. Unless otherwise noted, we will

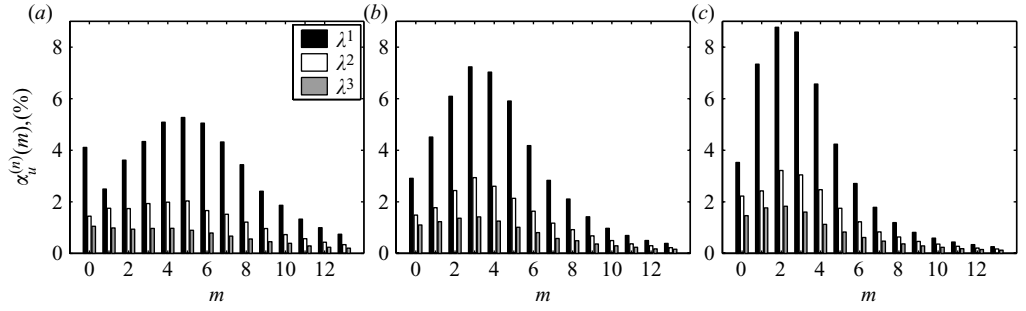

FIGURE 21. Azimuthal eigenspectra from the scalar decomposition of the axial component. (*a*) $x/D = 3.0$; (*b*) 5.0; (*c*) 8.0.

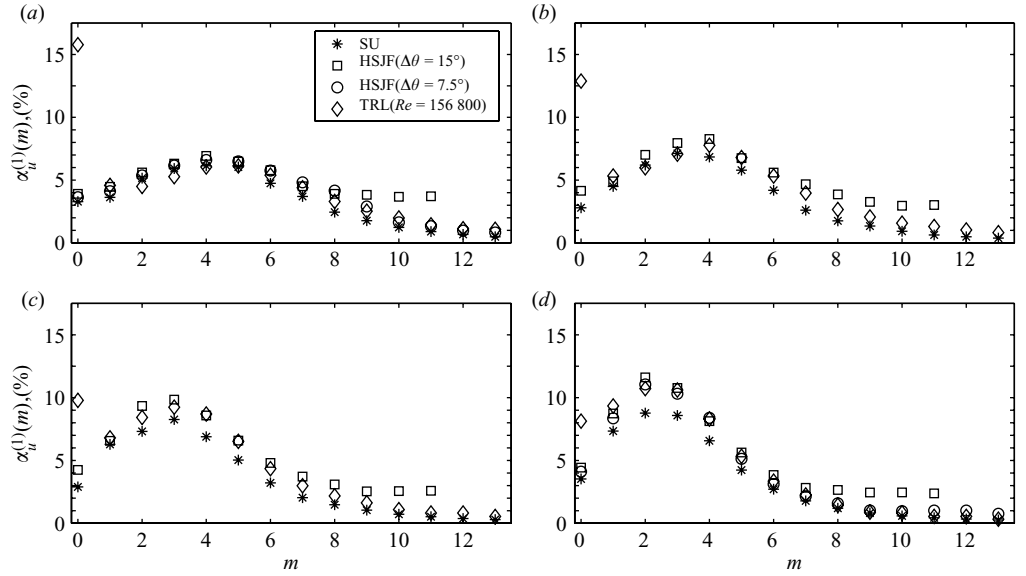

FIGURE 22. Azimuthal eigenspectra of the first POD mode from the scalar decomposition of the axial component. (*a*) $x/x_L = 0.6$; (*b*) 0.8; (*c*) 1.0; (*d*) 1.2.

confine the remainder of this discussion to the azimuthal mode number eigenspectra of the first POD eigenvalue.

In figures 22 to 24, the solutions from all three scalar implementations of the POD are shown alongside what is available in the literature; primarily confined to the work of Iqbal & Thomas (2007) and Jung *et al.* (2004). As the principal variation between these three studies comprises differences in the initial conditions (shear-layer thickness) or Mach-number-related effects, the axial position (x_L) where the centreline velocity reduces to 95 % of the jet exit velocity (see figure 7*a*) is used to normalize each axial position where the eigenspectra are computed; Reynolds-number effects should be negligible following the observations of Jung *et al.* (2004). Furthermore, as a coarse azimuthal grid can adversely effect the azimuthal eigenspectra (see Tinney, Glauser & Ukeiley 2005), both solutions from Iqbal & Thomas (2007) are presented, that is, for $\vartheta = 15^\circ$ and 7.5°.

The axial component eigenspectra are shown in figure 22 for the first POD mode and are found to agree reasonably well considering the range of Mach numbers (0.07

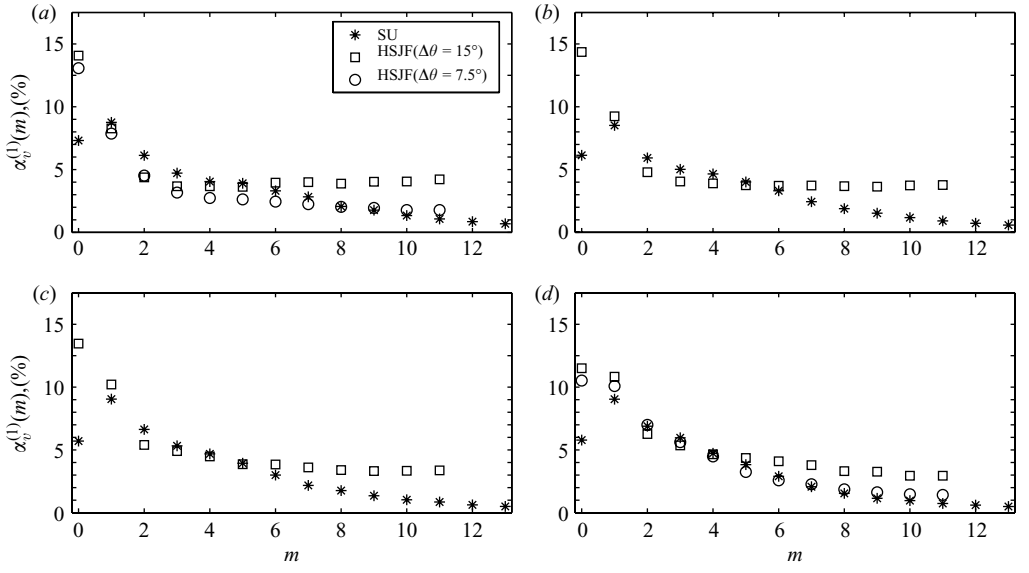

FIGURE 23. Azimuthal eigenspectra of the first POD mode from the scalar decomposition of the radial component. (*a*) $x/x_L = 0.6$, (*b*) 0.8, (*c*) 1.0, (*d*) 1.2.

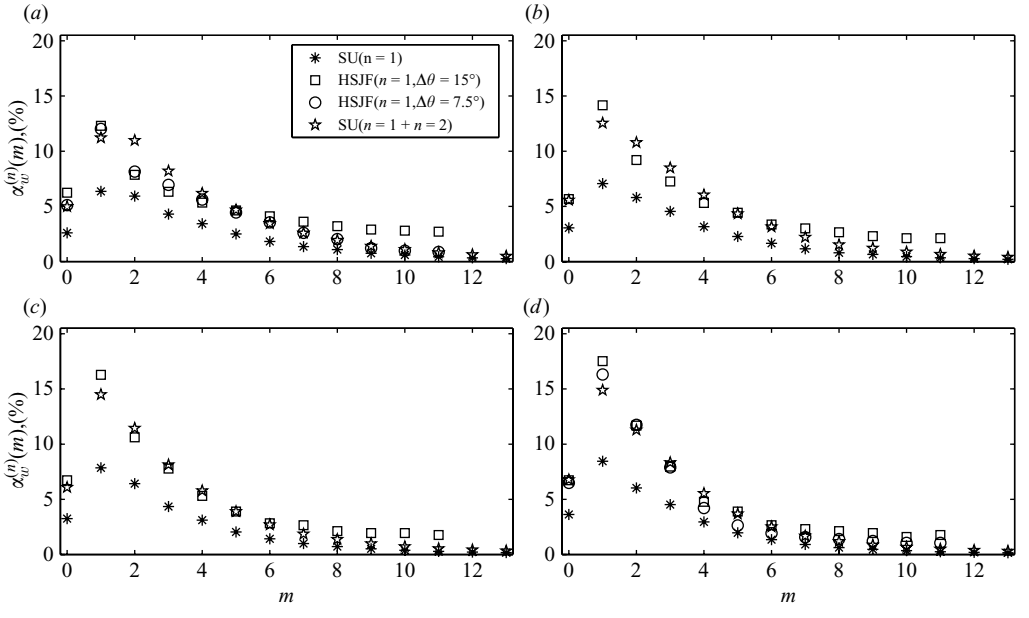

FIGURE 24. Azimuthal eigenspectra of the first POD mode from the scalar decomposition of the azimuthal component $\alpha_w^{(1)}(m)$. (*a*) $x/x_L = 0.6$; (*b*) 0.8; (*c*) 1.0; (*d*) 1.2. Also included is the summation of the first two POD modes $\alpha_w^{(1+2)}(m)$ from the current set of measurements.

to 0.85) that are being compared. Particularly striking is the rapid decay of the zero mode structure of Jung *et al.* (2004). Similar observations are shown in the current data set (figure 21*a*), but quickly become non-existent for the range of positions in figure 22. This appeared not to be the case for the Mach 0.30 measurements

of Iqbal & Thomas (2007). The axial component eigenspectra are otherwise quite complementary and are our first glimpse of the similarities in the structure between the low- and high-Mach-number subsonic jets.

Turning our attention to the radial component eigenspectra in figure 23, the sensitivity of the solutions from Iqbal & Thomas (2007) to the discretization of the azimuthal grid is much more important here; the smaller grid spacing (7.5°) being more complementary to the eigenspectra of the current Mach 0.85 data (4°). Where the dominant azimuthal mode number for the radial component's eigenspectra is concerned, a large discrepancy is found between the Mach 0.30 and Mach 0.85 data sets. The Mach 0.3 measurements of Iqbal & Thomas (2007) suggest that mode zero is dominant, whereas the current Mach 0.85 measurements indicate that it is the helical mode. A scalar decomposition of the radial component of velocity using the Mach 0.30 and 0.60 jet data of Ukeiley *et al.* (1999) showed that, for both Mach numbers, the helical mode was the dominant azimuthal mode through this region of the jet and is what we find here in the higher-Mach-number study.

Where the azimuthal component eigenspectra are concerned (figure 24), a deficiency in energy is clearly manifest in the first POD mode. Since the first two POD bases from the scalar decomposition of the azimuthal component have been found to turn towards harmonic functions, the first POD mode alone is not sufficient for representing the underlying large-scale characteristics of this component of the flow. However, the summation of the first two POD modes is sufficient and is shown in figure 24 to compare reasonably well (in energy) to the eigenspectra of Iqbal & Thomas (2007). The use of CTA wires to measure the fluctuations in the low-speed sides of the shear layer, where turbulence levels have been shown in figure 10 to go well beyond 50 % of the local mean value, results in irreversible rectifications of the signal. The consequence of this is an inability to properly capture the axial vorticity, which has been shown here from PIV surveys to be an important manifestation of the jet shear layer. It is conjectured that this is the leading cause of the disparities in energy between the solutions of Iqbal & Thomas (2007) and the current set of PIV measurements, and the lack of any mode number pairing in the solutions of Iqbal & Thomas (2007) for the scalar decomposition of the azimuthal component of velocity. Nevertheless, a consistency with both the current data set and the solutions of Iqbal & Thomas (2007) is observed in that the radial and azimuthal component eigenspectra are qualitatively similar (dominated by low azimuthal mode number energy) and have different eigenspectra shapes with respect to the axial component of velocity (rich in higher azimuthal mode number energy).

In view of the results from the vector decomposition in figure 25(a, b), the Fourier-azimuthal eigenspectra assimilate many of the features of the eigenspectra from the scalar decomposition of the axial component, but with less energy in the higher azimuthal modes. This is an effect of the much more lower-dimensional characteristics of the radial and azimuthal velocity components which have been shown here to suppress the energy in the higher Fourier-azimuthal modes when the full vector characteristics of the jet turbulence are considered. Thus with the vector decomposition, the azimuthal eigenspectra manifest an energy peak in mode 5 at $x/D = 3.0$ followed by a shift towards mode 2 by $x/D = 8.0$. The shape of the Fourier-azimuthal eigenspectra are more clearly represented when the first two most energetic POD eigenvalues are combined (figure 25b).

An attempt to reproduce the solutions of Iqbal & Thomas (2007) are shown in figure 25(a) by resampling the current high spatial-resolution Mach 0.85 PIV data onto a coarser grid ($\Delta\theta = 15°$, seven points in r where $\Delta r/D = 0.126$). The

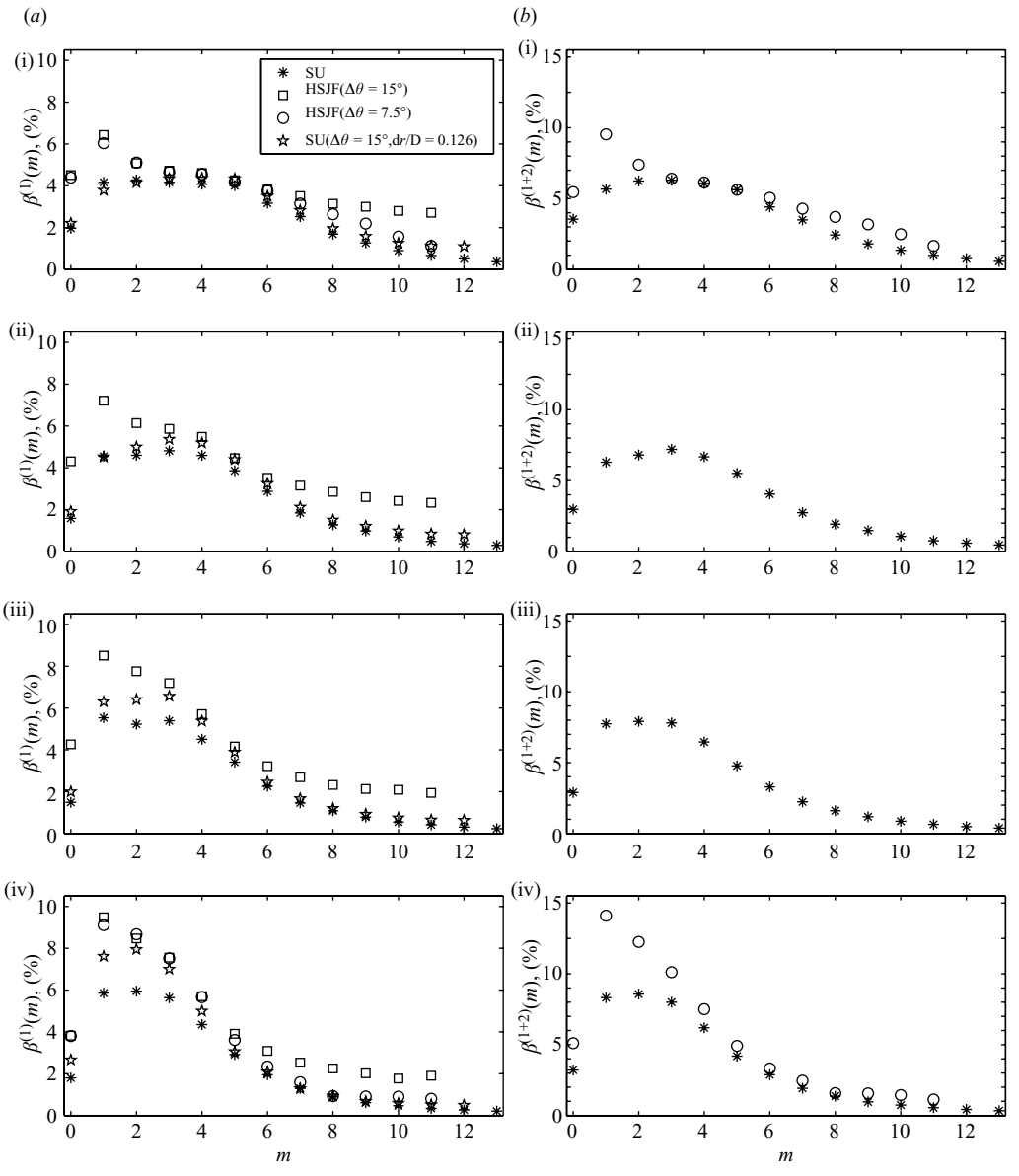

FIGURE 25. (*a*) Azimuthal eigenspectra of the first POD mode from the vector decomposition, $\beta^{(1)}(x;m)$. (*b*) Summation of the first two POD modes, $\beta^{(1+2)}(x;m)$. (i) $x/x_L = 0.6$; (ii) 0.8; (iii) 1.0; (iv) 1.2.

azimuthal eigenspectra of the first POD mode continues to resemble the current high-resolution trend, though with energy levels more comparable to the eigenspectra of Iqbal & Thomas (2007), especially in the downstream regions of the flow. This is counter-intuitive to what was found with the grid-sensitivity study. We would expect that the grossest over-estimates would occur in the near-nozzle region and decay with increasing axial position (for a fixed grid, both $\Delta r/\mathscr{L}_i$ and $\Delta r/\delta$ decrease as x increases). However, an additional adverse effect of the coarse measurement grid chosen by Iqbal & Thomas (2007) is its failure to capture the entire width of the shear

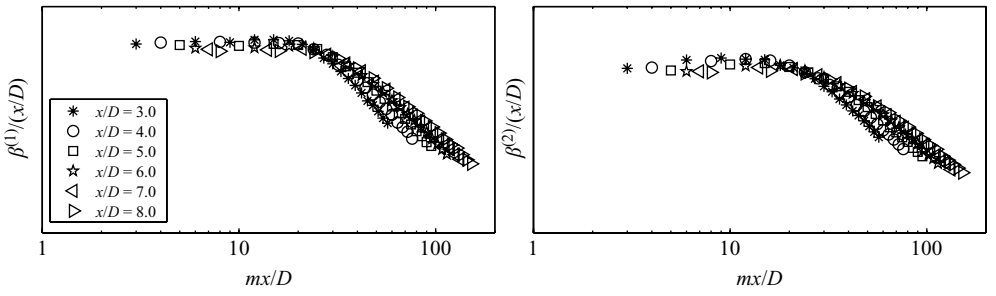

FIGURE 26. Scaled eigenspectra of the Fourier-azimuthal modes.

layer in the downstream regions of the flow; and so, any anticipated over-estimates in energy based on the findings reported in figure 20 are counteracted by the spatial confinement of the measurement grid to only a fraction of the shear layer, which is what we observe here when an attempt is made to reproduce the solutions of Iqbal & Thomas (2007). On account of the fidelity of the energy in the POD eigenvalues to the spatial grid's discretization, it is evident that the structure of the turbulent jet behaves similarly over a large range of Reynolds numbers and Mach numbers (subsonic).

Iqbal & Thomas (2007) have shown how the full three-dimensional jet structure stabilizes to a Fourier-azimuthal mode 1 in the transition region of the flow at $x/D = 12.0$. The subtle delay in the modal convergence to $m = 1$ at Mach 0.85 and $x/D = 8.0$ when compared to the lower-Mach-number jet is here attributed to the lengthening of the potential core at the much higher speeds (see figure 7). Although the dominance of the $m = 1$ mode in the far-field regions is shown to be small in comparison to the next higher mode, $m = 2$, it is nonetheless expected to occur here as well.

Scaling the normalized eigenspectra (4.12) of the Fourier-azimuthal modes with shear-layer variables is shown here in figure 26 to collapse the azimuthal eigenspectra of the first two POD modes from the vector decomposition. This was shown similarly by Taylor (2001) for the Mach 0.3 and 0.6 jet, and by Jung *et al.* (2004) for a range of lower-Reynolds-number jet flows.

4.3. *Low-order Fourier-azimuthal reconstructions of the kernel*

For completeness of discussion, the kernel is reconstructed using the first ($n = 1$) POD mode and the results from the scalar and vector decomposition to illustrate the spatial evolution of the Fourier-azimuthal modes of the most energetic radial flow structure. The results are computed using the following expression,

$$\mathscr{B}_{ii}^{(k)}(r, r', x; m) = \sum_{n=1}^{k} \lambda^{(n)}(x; m)\phi_i^{(n)}(r, x; m)\phi_i^{(n)}(r', x; m), \tag{4.13}$$

and are compared with reconstructions from the solution to the vector decomposition using (4.2). This is shown in figure 27 raised to the half power and normalized by the jet exit velocity. Like the Fourier-azimuthal modal distribution shown in figure 17, the radial distribution of modal energy reflects a spatial preference of the lower Fourier-azimuthal modes to the potential core regions of the flow, whereas the higher Fourier-azimuthal modes show the characteristics of the shear-layer and entrainment regions of the jet flow. Excellent agreement between the two results shows how the individual component features are preserved using the vector decomposition.

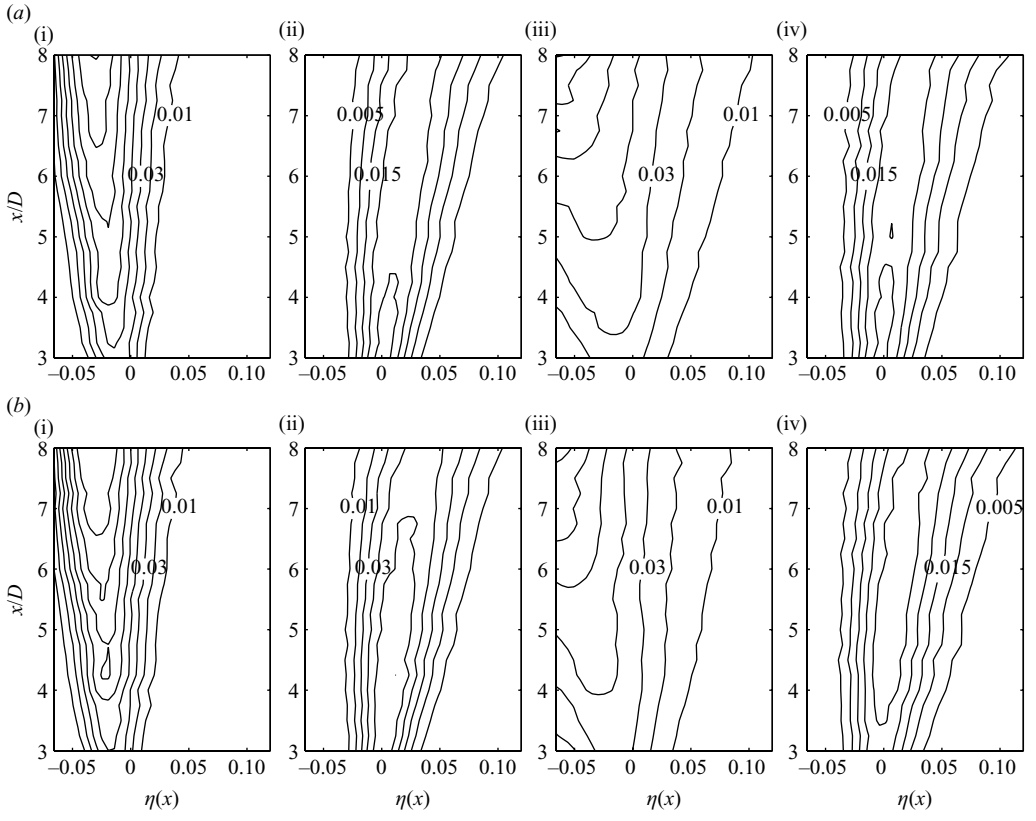

FIGURE 27. Eigenvector reconstructions of the axial and radial components of the kernel using *POD* mode 1 and Fourier-azimuthal modes 1 and 5 from the (*a*) scalar and (*b*) vector decompositions. (i) u, $m = 1$; (ii) 5; (iii) v, $m = 1$; (iv) 5.

The principal benefit of the vector POD is the ability to produce an optimal basis set which preserves orthogonality between both the POD modes and the different components of the velocity field that are included in the decomposition. Furthermore, the vector decomposition offers the opportunity of integrating shear stress terms into the basis set, those which are important for turbulence transport, vortex stretching and turbulence production, a necessary list of items that are essential for producing an accurate and stable low-order dynamical system model. There are, however, certain qualities about the scalar form of the technique which will be discussed in Part 2 as it pertains to a coupling of the POD basis from a decomposition of the velocity field, with a basis that is representative of the low-order features of the pressure field within the hydrodynamic periphery of the jet flow.

5. Snap-shots of the low-ordered flow events

Low-ordered reconstructions of the original instantaneous realizations along a slice in the (r, θ)-plane of the jet are performed using the most energetic modes from the vector POD. These are displayed at three axial positions in the flow ($x/D = 3.0$, 5.0 and 7.0) in figures 28 and 29 to demonstrate typical features of the most energetic flow events in physical space. In figure 28 the original snap-shots from the PIV system are shown for each velocity component, complemented by its corresponding

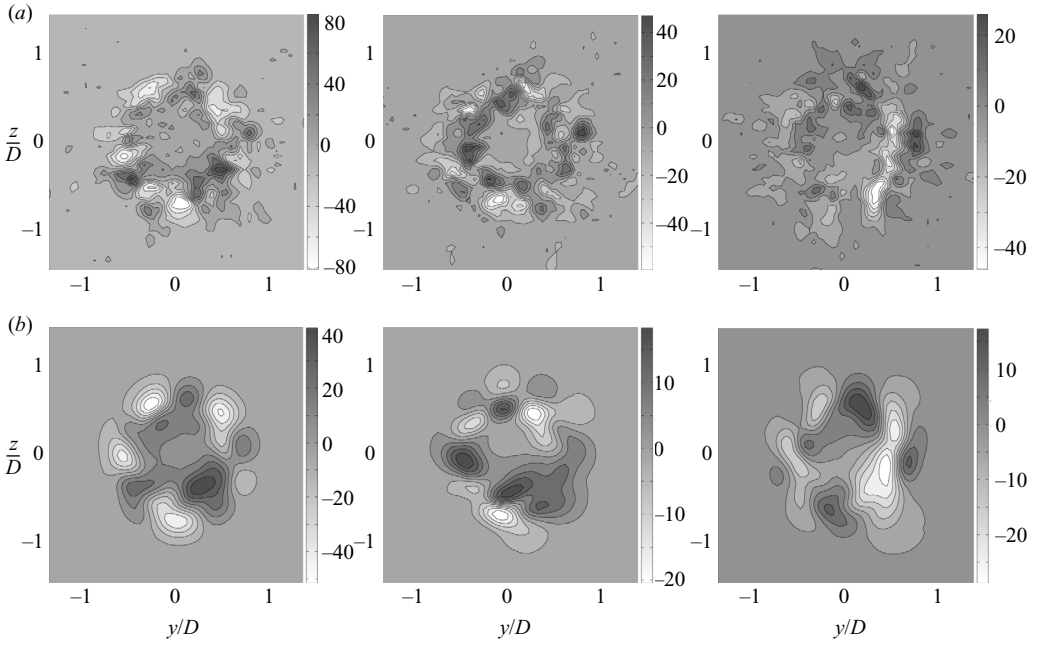

FIGURE 28. (*a*) PIV snap-shots of the axial, radial and azimuthal (left to right, respectively) components of the velocity field at $x/D = 3.0$, and (*b*) the corresponding low-ordered reconstruction using Fourier-azimuthal modes $m = 0$ to 6 and POD modes $n = 1$ to 3.

low-order ($n = 1$ to 3 and $m = 0$ to 6) reconstruction. In particular, the original and reconstructed snap-shot of the axial velocity at $x/D = 3.0$ illustrates a Fourier-azimuthal mode 5-like structure positioned along the centre of the shear layer. Likewise, radial and azimuthal components are shown to comprise similar modal behaviours.

Moving downstream to $x/D = 5.0$ and 7.0 in figure 29, three statistically independent time steps per position are shown. In this figure, the vector maps identify regions of axial vorticity (v, w components), while a grey-scale contour shows the topology of the axial velocity fluctuations (dark: positive, light: negative). Each of the six illustrations comprise velocity components that are phase aligned in time to provide a frozen picture of the full turbulent structures along a slice in the (r, θ)-plane of the jet. At $x/D = 5.0$, the higher Fourier modal events are still present along with a series of counter-rotating events, positioned along the centre of the jet's mixing layer near y/D and $z/D = 0.5$. By $x/D = 7.0$, the prominent energy-containing events of the flow cover a broader region in space, when compared to the flow topologies at $x/D = 3.0$ and 5.0. These events at $x/D = 7.0$ appear also to be less organized in their spatial distribution, as would be expected since the potential core has now collapsed. We can point to the regions of the flow where portions of the fluid mass are either entrained or ejected from the potential core. For example, the entrainment regions in the flow, located between two counter-rotating vortices, are shown (in all illustrations) to manifest negative streamwise fluctuations, thus characterizing the entrainment of a slower moving (relative to the local mean) mass of fluid into the jet core. Similar to the entrainment behaviour, the regions of fluid mass ejection, also identified by counter-rotating vortices (but opposite in sign), comprise positive streamwise fluctuations. Thus, the masses of fluid that are either entrained or ejected

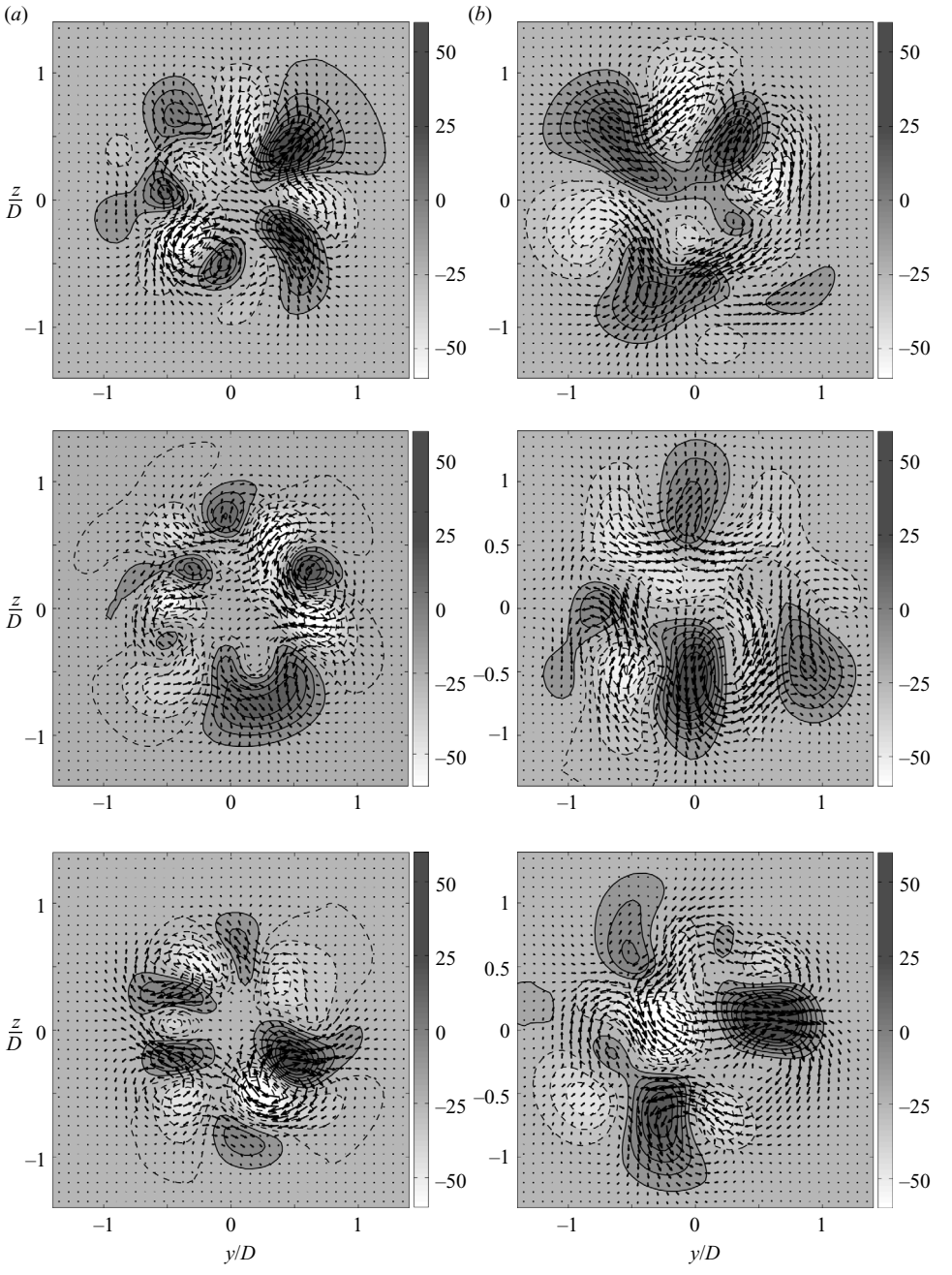

FIGURE 29. Low-order reconstructions at (*a*) $x/D = 5$ and (*b*) $x/D = 7$ from three statistically independent time steps (per position) using Fourier-azimuthal modes $m = 0$ to 6 and POD modes $n = 1$ to 3. The axial velocity is identified by grey-scale contours, while radial and azimuthal components (v, w) are represented in vector format.

manifest slow and fast-moving motions, respectively (see Hussain & Clark 1981, for a similar discussion using flow-visualization techniques).

An overall objective of employing low-order modelling techniques to turbulent flows is to separate the more energetic features of the flow field from the underlying random

motions in order to develop an intuition for the mechanisms responsible for most of the dynamical characteristics that govern the behaviour of these complex systems. Since the measurement techniques employed in this study compromised temporal resolution for spatial accuracy, the time dependences of these dynamical events are not available without having to perform additional work. To this end, the presentation and discussion of the measurements that have been presented here, form the basis for a concerted undertaking focused on reconstructing a time-dependent estimate of the most energetic turbulent features (from a turbulent kinetic energy point of view) of the jet using surveys of the near-field pressure via a spectral linear stochastic estimate procedure described by Ewing & Citriniti (1997) and Tinney *et al.* (2006*a*). From this low-dimensional estimate (presented in Part 2), the three-dimensional, time-resolved acoustic source terms are computed using all nine components of the Lamb vector and are propagated to several far-field observer positions using the analytical solution to Lighthill's (1952) formulation.

6. Summary

A Mach 0.85 flow exiting from a 50.8 mm axisymmetric converging nozzle into an anechoic chamber at ambient pressure and temperature was investigated experimentally using Pitot-tube, LDA and PIV instruments. Pitot-tube and LDA surveys of the axial velocity at the jet exit demonstrated a top-hat profile with an initial shear-layer thickness of $0.0175D$, and turbulence levels at $x/D = 0.5$ of the order of 1 %. The three-dimensional flow was surveyed along the (r, θ)-plane of the jet using a three-component PIV system between $x/D = 3.0$ and 8.0 ($\Delta x = 0.25D$). Spatial correlations were computed from the PIV measurements from which all nine normal and shear stress terms $R_{ij}(r, r', \vartheta; x)$ were determined at each axial station and across the entire (r, θ) measurement plane. The Fourier-azimuthal decomposition of all normal stresses showed once again that the potential core and high-speed sides of the mixing layer are characterized by the low Fourier-mode number events 1 and 2, whereas the low-speed side of the shear layer is governed by higher azimuthal mode events. In general, the radial and azimuthal components were much more low-dimensional than the axial component of the velocity field.

A proper orthogonal decomposition was performed using both scalar and vector forms of the technique. A grid-sensitivity study showed how the POD eigenvalues safely converge to within 1 % of their expected values when the ratio between the discretization of the measurement grid and the integral length scale is less than 0.3. On account of these disparities, the findings reported here agree reasonably well with the scalar decompositions reported by others at different Reynolds and Mach numbers, thus providing evidence that the structure of the turbulent jet behaves independently of these factors (under subsonic conditions and when the Reynolds number is sufficiently high).

Low-order reconstructions of the velocity field using only the most energetic turbulent flow events were shown alongside the original snap-shots from the PIV system at $x/D = 3.0,\ 5.0$ and 7.0. The reconstructions depict slow fluid entrainment into the jet's core and fast fluid ejection into the ambient field. Since the analysis comprised stationary measurements of statistically independent flow realizations in the (r, θ)-plane via PIV techniques, the dynamical characteristics of these events are unavailable which is important for understanding the mechanism by which the turbulent kinetic energy of the flow is converted into sound energy. Thus, in Part 2, an effort is made using stochastic estimation methods to produce time-varying POD coefficients which are capable of making a three-dimensional, three-component

time-resolved estimate of the low-order flow events that manifest the near-field and early transition regions of this Mach 0.85 jet flow.

The authors gratefully acknowledge the financial support of Syracuse University and the Air Force Office of Scientific Research. In addition, the authors would like to acknowledge William K. George, Maja Wänström and Joël Delville for many helpful discussions and to André M. Hall for acquiring the LDA measurements. A great portion of this work was written while C. E. T. was a resident at the Laboratoire d'Etudes Aérodynamiques in Poitiers, France and being supported by a fellowship from the Centre National de la Recherche Scientifique.

REFERENCES

Adrian, R. J. 1991 Particle-imaging techniques for experimental fluid mechanics. *Annu. Rev. Fluid. Mech.* **23**, 261–304.

Adrian, R. J. & Yao, C. S. 1986 Power spectra of fluid velocities measured by laser Doppler velocimetry. *Exps. Fluids* **5**, 17–28.

Agüí, J. C. & Jiménez, J. 1987 On the performance of particle tracking. *J. Fluid Mech.* **185**, 447–468.

Alkislar, M. B., Krothapalli, A. & Butler, G. W. 2007 The effect of streamwise vortices on the aeroacoustics of a Mach 0.9 jet. *J. Fluid Mech.* **578**, 139–169.

Arakeri, V. H., Krothapalli, A., Siddavaram, V., Alkislar, M. B. & Lourenco, L. M. 2003 On the use of microjets to suppress turbulence in a Mach 0.9 axisymmetric jet. *J. Fluid Mech.* **490**, 75–98.

Aubry, N., Holmes, P., Lumley, J. & Stone, E. 1988 The dynamics of coherent structures in the wall region of a turbulent boundary layer. *J. Fluid Mech.* **192**, 115–173.

Bastin, F., Lafon, P. & Candel, S. 1997 Computation of jet mixing noise due to coherent structures: the plane jet case. *J. Fluid Mech.* **335**, 261–304.

Berkooz, G., Holmes, P. & Lumley, J. L. 1993 The proper orthogonal decomposition in the analysis of turbulent flows. *Annu. Rev. Fluid Mech.* **25**, 539–575.

Bonnet, J. P., Delville, J., Glauser, M. N., Antonia, R. A., Bisset, D. K., Cole, D. R., Fiedler, H. E., Garem, J. H., Hilberg, D., Jeong, J., Kevlahan, N. K. R., Ukeiley, L. S. & Vincendeau, E. 1998 Collaborative testing of eddy structure identification methods in free turbulent shear flows. *Exps. Fluids* **25**, 197–225.

Bradshaw, P., Ferriss, D. H. & Johnson, R. F. 1964 Turbulence in the noise-producing region of a circular jet. *J. Fluid Mech.* **19**, 591–624.

Bridges, J. 2006 Effect of heat on space–time correlations in jets. *AIAA Paper* 2006-2534.

Brown, G. L. & Roshko, A. 1974 Density effects and large structure in turbulent mixing layers. *J. Fluid Mech.* **64**, 775–816.

Caraballo, E., Samimy, M., Scott, J., Narayanan, S. & DeBonis, J. 2003 Application of proper orthogonal decomposition to a supersonic axisymmetric jet. *AIAA J.* **41**, 1–12.

Citriniti, J. H. & George, W. K. 1997 The reduction of spatial aliasing by long hot-wire anemometer probes. *Exps. Fluids* **23**, 217–224.

Citriniti, J. H. & George, W. K. 2000 Reconstruction of the global velocity field in the axisymmetric mixing layer utilizing the proper orthogonal decomposition. *J. Fluid Mech.* **418**, 137–166.

Delville, J. 1994 Characterization of the organization in shear layers via the proper orthogonal decomposition. *Appl. Sci. Res.* **53**, 263–281.

Delville, J., Ukeiley, L., Cordier, L., Bonnet, J. P. & Glauser, M. N. 1999 Examination of large scale structures in a turbulent plane mixing layer. Part 1. Proper orthogonal decomposition. *J. Fluid Mech.* **391**, 91–122.

Dosanjh, D. S., Bhutiani, P. K. & Ahuja, K. K. 1977 Supersonic jet noise suppression by coaxial multi-nozzle cold/heated jet flows. *Dept of Transportation Final Rep., Washington DC*, March, 1977.

Ewing, D. & Citriniti, J. 1999 Examination of a LSE/POD complementary technique using single and multi-time information in the axisymmetric shear layer. *Proc. IUTAM Symp. Lynby, Denmark, 25–29 May, 1997* (ed. J. N. Sorensen, E. J. Hopfinger & N. Aubry), pp. 375–384. Kluwer.

Ffowcs Williams, J. E. & Kempton, A. J. 1978 The noise from the large scale structure of a jet. *J. Fluid Mech.* **84**, 673–694.

Freund, J. B. 2001 Noise sources in a low-Reynolds-number turbulent jet at Mach 0.9. *J. Fluid Mech.* **438**, 277–305.

Freund, J. B. & Colonius, T. 2002 POD analysis of sound generation by a turbulent jet. *AIAA Paper* 2002-0072.

Gamard, S., Jung, D. & George, W. K. 2004 Downstream evolution of the most energetic modes in a turbulent axisymmetric jet at high Reynolds number. Part 2. The far-field region. *J. Fluid Mech.* **514**, 205–230.

George, W. K., Beuther, P. D. & Arndt, R. E. A. 1984 Pressure spectra in turbulent free shear flows. *J. Fluid Mech.* **148**, 155–191.

Glauser, M. N. 1987 Coherent structures in the axisymmetric turbulent jet mixing layer. PhD Dissertation, State University of New York at Buffalo. Amherst.

Glauser, M. N. & George, W. K. 1987 Orthogonal decomposition of the axisymmetric jet mixing layer including azimuthal dependence. *Advances in Turbulence* (ed. G. Comte-Bellot & J. Mathieu), pp. 357–366. Springer.

Glauser, M. N. & George, W. K. 1992 Application of multipoint measurements for flow characterization. *Expl Thermal Fluid Sci.* **11**, 617–632.

Guitton, A., Tinney, C. E., Jordan, P. & Delville, J. 2007 Measurements in a co-axial subsonic jet. *AIAA Paper* 2007-0015.

Hall, A. M., Glauser, M. N. & Tinney, C. E. 2005 Experimental investigation of the pressure–velocity correlation of an $M = 0.6$ axisymmetric jet. *AIAA Paper* 2005-5294.

Hussain, A. K. M. F. & Clark, A. R. 1981 On the coherent structure of the axisymmetric mixing layer: a flow-visualization study. *J. Fluid Mech.* **104**, 263–294.

Hussein, H. J., Capp, S. P. & George, W. K. 1994 Velocity measurements in a high Reynolds-number, momentum-conserving, axisymmetric turbulent jet. *J. Fluid Mech.* **258**, 31–75.

Iqbal, M. O. & Thomas, F. O. 2007 Coherent structures in a turbulent jet via a vector implementation of the proper orthogonal decomposition. *J. Fluid Mech.* **571**, 281–326.

Jung, D., Gamard, S. & George, W. K. 2004 Downstream evolution of the most energetic modes in a turbulent axisymmetric jet at high Reynolds number. Part 1. The near-field region. *J. Fluid Mech.* **514**, 173–204.

Juve, D., Sunyach, M. & Comte-Bellot, G. 1980 Intermittency of the noise emission in subsonic cold jets. *J. Sound Vib.* **71**:3, 319–332.

Keane, R. D. & Adrian, R. J, 1992 Theory of cross-correlation analysis of PIV images. *Appl. Sci. Res.* **49**, 191–215.

Kerhervé, F., Jordan, P., Gervais, Y., Valière, J. C. & Braud, P. 2004 Two-point laser Doppler velocimetry measurements in a Mach 1.2 cold supersonic jet for statistical aeroacoustic source model. *Exps. Fluids* **37**, 419–437.

Lau, J. C., Morris, P. J. & Fisher, M. J. 1979 Measurements in subsonic and supersonic free jets using a laser velocimeter. *J. Fluid Mech.* **93**, 1–27.

Lighthill, M. J. 1952 On sound generated aerodynamically: general theory. *Proc. R. Soc. Lond.* **211**, 564–587.

Lumley, J. L. 1967 The structure of inhomogenous turbulent flows. In *Atmospheric Turbulence and Radio Wave Propagation* (ed. A. M. Yaglom & V. I. Tatarski), pp. 166–178. Nauka, Moscow.

Meinhart, C. D. & Wereley, S. T. 2003 Theory of diffraction-limited resolution in micro particle image velocimetry. *Meas. Sci. Technol.* **14**, 1047–1053.

Melling, A. 1997 Tracer particles and seeding for particle image velocimetry. *Meas. Sci. Technol.* **8**, 1406–1416.

Meyers, J. F. 1991 Generation of particles and seeding. *Von Karman Inst. Fluid Dyn.* **8**, 1–42.

Michalke, A. & Fuchs, H. V. 1975 On turbulence and noise of an axisymmetric shear flow. *J. Fluid Mech.* **70**, 179–205.

Moin, P. & Moser, R. D. 1989 Characteristic eddy decomposition of turbulence in a channel. *J. Fluid Mech.* **200**, 471–509.

Morris, P. J. 1976 Turbulence measurements in subsonic and supersonic axisymmetric jets in a parallel stream. *AIAA J.* **14**, 1468–1475.

Narayanan, S., Barber, T. J. & Polak, D. R. 2002 High subsonic jet experiments: turbulence and noise generation studies. *AIAA J.* **40**, 430–437.

Noack, B. R., Papas, P. & Monkewitz, P. A. 2005 The need for a pressure-term representation in empirical Galerkin models of incompressible shear flows. *J. Fluid Mech.* **523**, 339–365.

Raffel, M., Willert, C. & Kompenhans, J. 1998 *Particle Image Velocimetry*. Springer.

Ribner, H. S. 1969 Quadrupole correlations governing the pattern of jet noise. *J. Fluid Mech.* **38**, 1–24.

Seiner, J. 1998 A new rational approach to jet noise reduction. *Theor. Comput. Fluid Dyn.* **10**, 373–383.

Sirovich, L. 1987 Turbulence and the dynamics of coherent structures. Part I. Coherent structures. *Q. Appl. Maths* **45**, 561–571.

Stromberg, J. L., McLaughlin, D. K. & Trout, T. R. 1980 Flow field and acoustic properties of a Mach number 0.9 jet at low Reynolds number. *J. Sound Vib.* **72**, 159–176.

Tam, C. K. W. 1998 Jet Noise: Since 1952. *Theor. Comput. Fluid Dyn.* **10**, 393–405.

Taylor, J. A. 2001 Dynamics of large scale structures in turbulent shear layers. PhD Dissertation, Clarkson University Rep. MAE-354, Potsdam, NY.

Taylor, J. T., Ukeiley, L. S. & Glauser, M. N. 2001 A low-dimensional description of the compressible axisymmetric shear layer. *AIAA Paper* 2001-0292.

Tennekes, H. & Lumley, J. L. 1972 *A First Course in Turbulence*. MIT Press.

Tinney, C. E. 2005 Low-dimensional techniques for sound source identification in high speed jets. PhD Dissertation, Syracuse University, Syracuse.

Tinney, C. E. & Jordan, P. 2008 The near-field pressure surrounding co-axial subsonic jets. *J. Fluid Mech.* **611**, 175–204.

Tinney, C. E., Hall, A., Glauser, M. N., Ukeiley, L. S. & Coughlin, T. 2004 Designing an anechoic chamber for the experimental study of high speed heated jets. *AIAA Paper* 2004-0010.

Tinney, C. E., Glauser, M. N. & Ukeiley, L. S. 2005 The evolution of the most energetic modes in a high subsonic Mach number turbulent jet. *AIAA Paper* 2005-0417.

Tinney, C. E., Coiffet, F., Delville, J., Glauser, M., Jordan, P. & Hall, A. 2006*a* On spectral linear stochastic estimation. *Exps. Fluids* **41**, 763–775.

Tinney, C. E., Glauser, M. N., Eaton, E. & Taylor, J. A. 2006*b* Low-dimensional azimuthal characteristics of suddenly expanding axisymmetric flows. *J. Fluid Mech.* **567**, 141–155.

Tinney, C. E., Jordan, P., Delville, J., Hall, A. M. & Glauser, M. N. 2006*c* A time-resolved estimate of the turbulence and sound source mechanisms in a subsonic jet flow. *J. Turbulence* **8**, 1–20.

Tinney, C. E., Ukeiley, L. S. & Glauser, M. N. 2008 Low-dimensional characteristics of a transonic jet. Part 2. Estimate and far-field prediction. *J. Fluid Mech.* (in press).

Townsend, A. A. 1956 The structure of turbulent shear flow, 2nd edn. Cambridge University Press.

Ukeiley, L. S. & Ponton, M. K. 2004 On the near field pressure of a transonic axisymmetric jet. *Intl J. Aeroacoust.* **3**, 43–66.

Ukeiley, L., Seiner, J. & Ponton, M. 1999 Azimuthal structure of an axisymmetric jet mixing layer. *ASME FEDSM* 99-7252.

Ukeiley, L., Cordier, L., Manceau, R., Delville, J., Glauser, M. N. & Bonnet, J. P. 2001 Examination of large scale structures in a turbulent plane mixing layer. Part 2. Dynamical systems model. *J. Fluid Mech.* **441**, 67–108.

Ukeiley, L. S., Tinney, C. E., Mann, R. & Glauser, M. N. 2007 Spatial correlations in a transonic jet. *AIAA J.* **45**, 1357–1369.

Wänström, M., George, W. K. & Meyer, K. E. 2006 Stereoscopic PIV and POD applied to the far turbulent axisymmetric jet. *AIAA Paper* 2006-3368.

Westerweel, J. 1998 Effect of sensor geometry on the performance of PIV interrogation. *Laser Techniques Applied to Fluid Mech*, 9*th Intl Symp., Lisbon, Portugal*, pp. 37–55. Springer.

Westerweel, J., Dabiri, D. & Gharib, M. 1997 The effect of a discrete window offest on the accuracy of cross-correlation analysis of digital PIV recordings. *Exps. Fluids* **23**, 20–28.

Willert, C. E. & Gharib, M. 1991 Digital particle image velocimetry. *Exps. Fluids* **10**, 181–193.

Wills, J. A. B. 1964 On convection velocities in turbulent shear flows. *J. Fluid Mech.* **20**, 417–432.

Winant, C. D. & Browand, F. K. 1974 Vortex pairing: the mechanism of turbulent mixing layer growth at moderate Reynolds number. *J. Fluid Mech.* **63**, 237–255.